Geochronological and geochemical studies of the metasedimentary rocks and diabase from the Jingtieshan deposit, North Qilian, NW China: Constraints on the associated banded iron formations

Xiuqing Yang [a,b,*], Zuoheng Zhang [c], Shaofeng Guo [d], Jie Chen [e], Dachuan Wang [e]

[a] School of Earth and Space Sciences, Peking University, Beijing 100871, China
[b] MLR Key Laboratory of Metallogeny and Mineral Assessment, Institute of Mineral Resources, Chinese Academy of Geological Sciences, Beijing 100037, China
[c] Chinese Academy of Geological Sciences, Beijing 100037, China
[d] Research and Development Center, China Geological Survey, Beijing 100037, China
[e] State Key Laboratory of Geological Process and Mineral Resources, China University of Geosciences, Beijing 100083, China

ARTICLE INFO

ABSTRACT

The Jingtieshan banded iron formations (JBIFs), located in the western segment of the North Qilian area, are one of the major iron deposits in NW China. The BIF occurs within the Jingtieshan Group intercalated with metasedimentary rocks which have undergone lower greenschist-facies metamorphism, and were intruded by a series of diabase sills/dykes. Here we present U–Pb data on detrital zircons from the metasedimentary rocks and the results show ages ranging from 1331 to 2919 Ma. Zircons from two diabase samples yield emplacement ages of 1236 ± 3 Ma (n = 10, MSWD = 0.26) and 1234 ± 7 Ma (n = 19, MSWD = 0.55), respectively. These new data constrain the depositional age of the JBIF at 1.23–1.33 Ga. The geochemical characteristics (e.g., CIA, PIA, Al_2O_3/TiO_2, trace element ratios and REE patterns) of the metasedimentary rocks indicate that the protolith sediments were mainly sourced from mafic and intermediate igneous rocks, followed by post-depositional K-metasomatism. The prominent age peak at 1747 Ma obtained from detrital zircons in the metasediments suggests that the zircons were mostly sourced from the underlying Zhulongguan Group in North Qilian area. The subordinate population of Early Mesoproterozoic detrital zircons was probably sourced from the North Qilian area. The minor population of zircons with Archean ages was derived from the Archean basement in the neighboring old craton. The diabase samples are characterized by slight LREE enrichment, display no distinct Eu and Ce anomalies, and show enrichment in Rb, Ba, K, and Pb and depletion in Nb, Ta, and Sr. These features suggest that the primary magmas of the diabases were likely generated by partial melting of the transitional mantle. The data presented in this study suggest that the JBIF formed in a continental margin sea within an extensional setting.

1. Introduction

Banded iron formations (BIFs) are sedimentary units deposited mostly during Archean–Paleoproterozoic (3.8–1.8 Ga) and less commonly during Neoproterozoic (0.8–0.6 Ga) (Klein, 2005; Holland, 2005; Ilyin, 2009). It is well established that the level of atmospheric oxygen was extremely low before 2.45 Ga ago. The rise of atmospheric oxygen occurred 2.4 billion years ago, and developed a stable and oxygenated atmospheric in Phanerozoic eon (less than 542 million years ago) (Bekker et al., 2004; Arnold et al., 2004; Planavsky et al., 2011; Reinhard et al., 2013; Lyons et al., 2014). However, the redox states of the mid-Proterozoic ocean are less well known. Large-scale occurrence of BIF deposits is rare during the age gap of 1.8 to 0.8 Ga,

although several BIFs with VHMS and SEDEX deposits such as the Broken Hill (Richards, 1966; Lascelles, 2014) and Pecos greenstone belt in New Mexico (Slack et al., 2009) have been well documented. The absence of BIF between 1.8 and 0.8 Ga has been explained by either complete ocean oxidation (Holland, 1984, 2003) or by development of sulfidic conditions in the deep ocean (Canfield, 1998; Poulton et al., 2004). Both models also explain the redox state of the mid-Proterozoic. More recently, a new model of ferruginous (anoxic and iron-rich) conditions in the deep water during the mid-Proterozoic ocean has been proposed (Bekker et al., 2010; Planavsky et al., 2011; Poulton and Canfield, 2011; Pufahl et al., 2013; Lyons et al., 2014).

In north-western China, voluminous Mesoproterozoic Jingtieshan-type BIF deposits occur in the North Qilian area, within the Jingtieshan Group in the Gansu Province (Sun et al., 1998; Zhou and Yue, 1999; Mao et al., 2003; 2012; Zhang et al., 2014; Li et al., 2014, 2015a). The Jingtieshan BIF (JBIF), the largest and best-preserved Mesoproterozoic BIF, is hosted within meta-clastic-carbonate sedimentary formations,
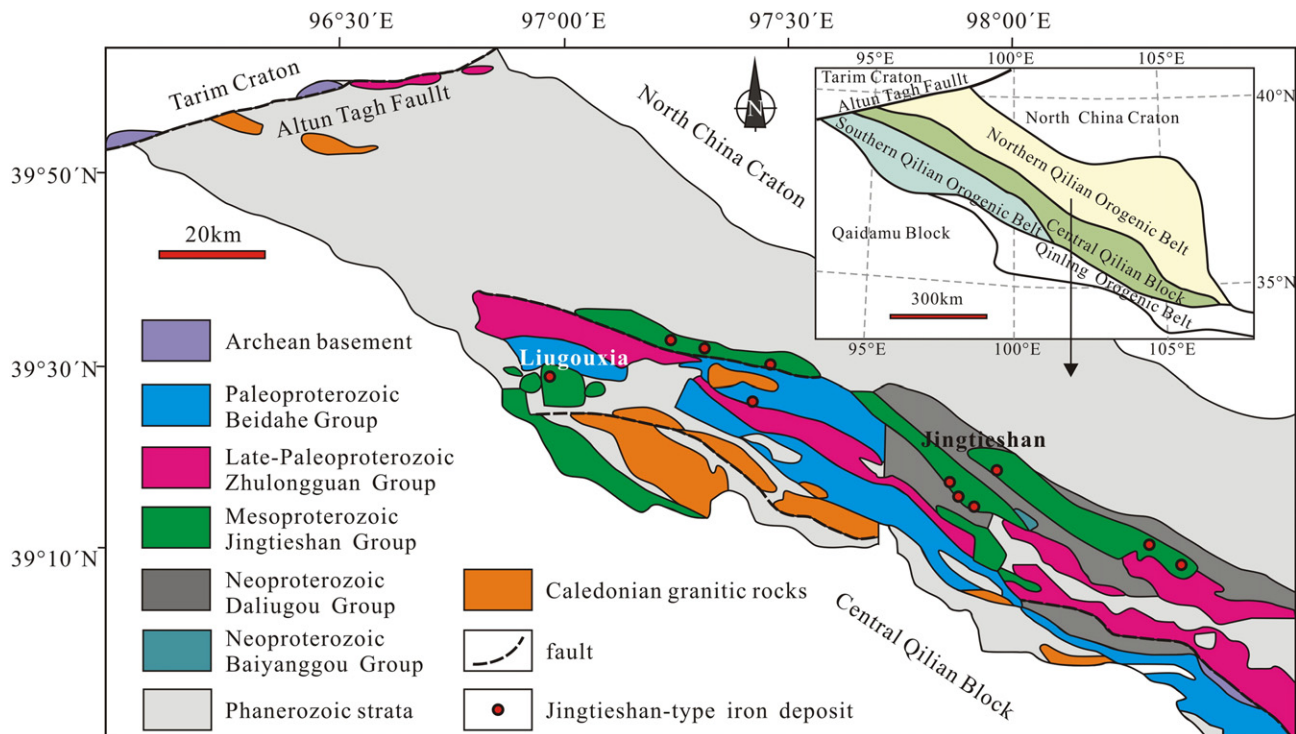
Fig. 1. Geological map of the western segment of North Qilian area, China (modified from Mao et al., 1997).

and provides a typical example to evaluate the formation of Mesoproterozoic BIF in China. The JBIF consists of alternating iron-rich (specularite/hematite and siderite), silica-rich, and barite-rich layers with high contents of $Fe_2O_3^t$, SiO_2 and BaO. The BIF also shows negative $\delta^{13}C$ values of siderite, positive Eu anomalies, and lack significant

negative Ce anomalies, suggesting that the ore-forming material was derived from submarine hydrothermal solutions with weak seawater signature in anoxic deep-water (Yang et al., 2015). However, precise geochronological data are lacking for the JBIF, and the proposed Mesoproterozoic depositional age comes from relatively poor regional

Era&Period	Stratum	Histogram	Thickness (m)	Lithology	Age
Neoproterozoic	Baiyanggou Group		1075	Conglomerate rock.	
	Daliugou Group		4500	Siltstone, marlstone, dolomite, basalt, K-rich marstone, dolomite limestone, argillaceous, carbonaceous slate, motley argillaceous limestone and limestone conglomerates.	
Mesoproterozoic	Jingtieshan Group		6000	Upper lithostratigraphic units: dolomitic marble. Lower lithostratigraphic units: phyllite, BIF and quartzite.	1.23~1.33Ga This study
Paleoproterozoic	Zhulongguan Group		2055	Pillow basic lava, basic dike swarm, intermediate-mafic lava, volcanic breccia, tuff, slate, limestone, siliceous rock, sandstone and iron deposit.	1770~1840Ma Xu et al., 1996 Mao et al., 1997 Zhang et al., 2001
	Beidahe Group		>6000	Gnesis, schist, amphibolite, marble, dolostone and miner BIF.	1980±2.7 Ma Mao et al., 2003

Fig. 2. Generalized Precambrian stratigraphy of the North Qilian area, China (modified from Mao et al., 2003).
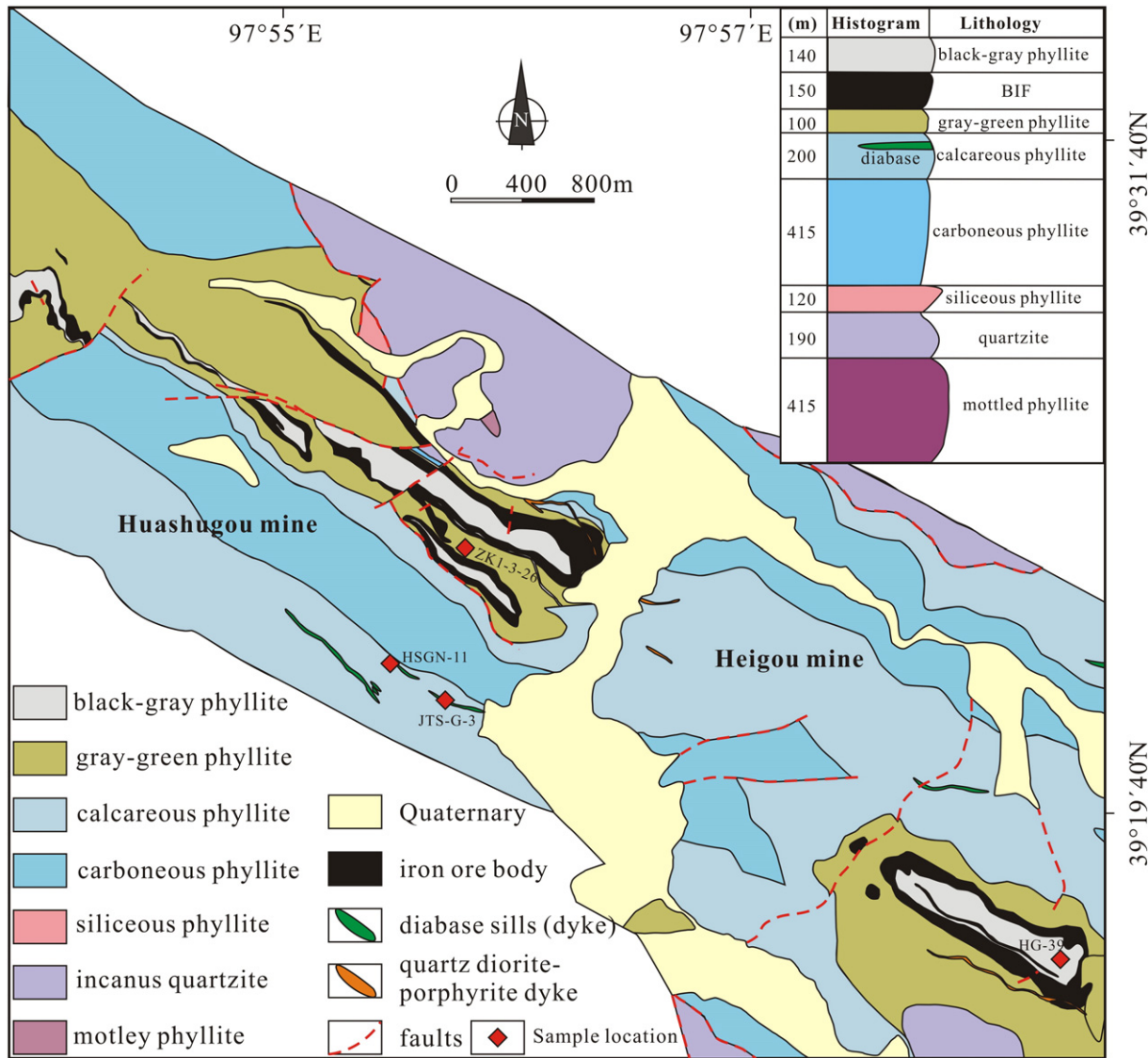
Fig. 3. Geological map of Jingtieshan iron deposit in Gansu province, China (after Liu et al., 1998), and the inserted stratigraphic histogram of the Jingtieshan group are from Sun et al. (1998).

correlation (e.g., Zhang et al., 2001; Mao et al., 2003, 2012) and imprecise Sm–Nd whole rock isochron age (Yang and Zhao; 1999).

In this study, we present zircon U–Pb dating and geochemical data on the metasedimentary rocks which are interstratified with BIF, and associated diabase dykes which were emplaced into the Jingtieshan Group from the Jingtieshan iron deposit. These new data allow us to better constrain the formation age of the JBIF as well as its relevance to the geotectonic setting in North Qilian area.

2. General geology

The NWW-trending Northern Qilian Orogenic Belt (NQOB) is part of the Qinling–Qilian–Kunlun Fold Systems (Mao et al., 2003; Song et al., 2013; Huang et al., 2015). The NQOB is bound by the North China Craton (NCC) to the northwest, by the Tarim Craton to the west, and by the Central Qianlian Block to the south (Fig. 1). The NQOB is considered to represent a typical oceanic suture zone and is composed of, Precambrian basement, Neoproterozoic to Early Paleozoic ophiolite sequences, HP metamorphic belts, island-arc volcanic rocks and granitoid plutons, Silurian flysch formations, Devonian molasse, and Carboniferous to Triassic sedimentary cover sequences (Song et al., 2013; Huang et al., 2015; Ker et al., 2015). The Precambrian basement occurs as relict micro

blocks, especially in the western segment of the NQOB (Zuo et al., 2002). The Precambrian lithology of the NQOB is composed of the Paleoproterozoic Beidahe Group, Late Paleoproterozoic Zhulongguan Group, Mesoproterozoic Jingtieshan Group, Neoproterozoic Daliugou Group and Baiyanggou Group (Fig. 2) (Zhang et al., 1998, 2001; Xia et al., 1999; Mao et al., 2003). The Beidahe Group is the oldest crystalline basement. Mao et al. (2003) reported Sm–Nd isochron ages of 1980 ± 2.7 Ma for this unit. The Zhulongguan Group lies unconformably over the Beidahe Group, with Sm–Nd isochrones ages of 1770.9 ± 333.0 Ma (Xu et al., 1996), single zircon U–Pb ages of 1783 to 1840 Ma (Mao et al., 1997), and zircon SHRIMP U–Pb ages of 1777 Ma (Zhang et al., 2001). This in turn is unconformably overlain by the Jingtieshan Group with age of 1309 ± 80 Ma (whole rock Sm–Nd isochron ages of BIF, Yang and Zhao, 1999), although Late Neoproterozoic ages have also been reported (Yang et al., 1991; Xue et al., 1997). The overlying Neoproterozoic Daliugou and Baiyanggou Group, show fault contact with the Jingtieshan Group.

The Paleoproterozoic–Archean basement of NQOB has been considered to have undergone continental rifting, initiated in the early Mesoproterozoic (e.g., Xu et al., 1996; Zhang et al., 1998), and continued until Neoproterozoic accompanied by the emplacement of bimodal volcanic rocks. Following the Late Neoproterozoic final breakup of the
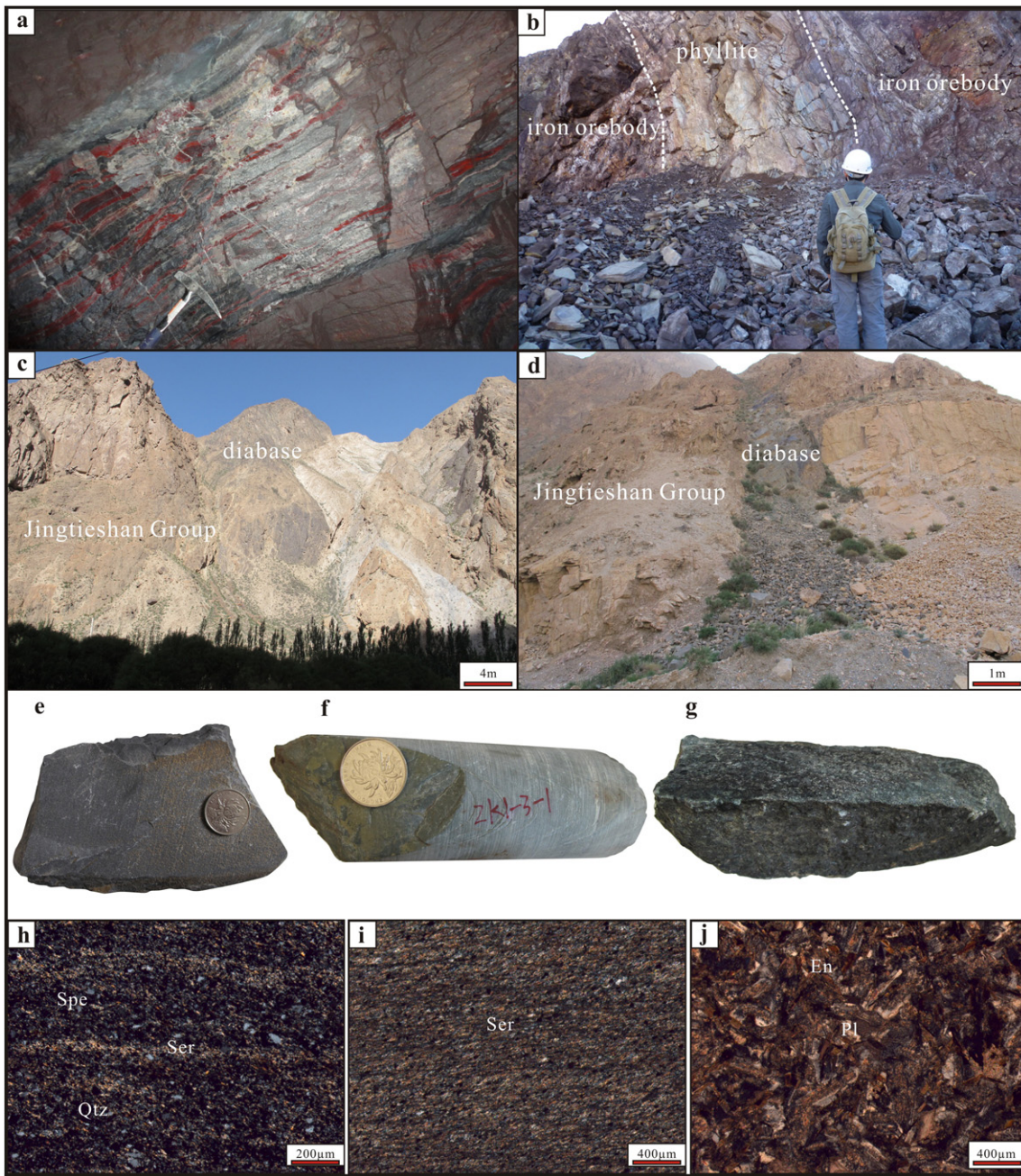
Fig. 4. Field photographs and photomicrographs of the phyllite and diabase in Jingtieshan Group. (a) The stratiform iron orebody. (b) Phyllite interlayered with the iron orebody. (c–d) Field occurrence of diabase dyke, and its location in Fig. 3. (e) Hand specimen of black–gray phyllite (HG-39). (f) Hand specimen of gray–green phyllite (ZK1-3-26). (g) Hand specimen of diabase (HSGN-11). (h) Photomicrographs of black–gray phyllite under crossed nicols. (i) Photomicrographs of gray–green phyllite under crossed nicols. (j) Photomicrographs of diabase under crossed nicols. Spe—specularite; Ser—sericite; Qtz—quartz; Pl—plagioclase, En—edenite.

NQOB which has been correlated to the breakup of the supercontinent Rodinia, and formation of the Qilian ocean (Xia et al., 1996, 1999; Song et al., 2013), orogenic activity was initiated in the Middle Cambrian and was active until the closure of the ancient Qilian ocean, with subduction during early Paleozoic (e.g., Xu et al., 1994; Xia et al., 1996, 2003; Wu et al., 2011).

The Jingtieshan iron deposit is located in the western segment of NQOB, including the Huashugou and Heigou mines (Fig. 3). In the Jingtieshan area, the lower lithostratigraphic units of the Jingtieshan Group and Quaternary formation have been identified. The lower lithostratigraphic units of the Jingtieshan Group, which have been metamorphosed to low greenschist facies, are composed of motley phyllite (jt_{1-1}), incanus quartzite (jt_{1-2}), siliceous phyllite (jt_{1-3}), carbonaceous phyllite (jt_{1-4}), calcareous phyllite (jt_{1-5}), gray–green phyllite (jt_{1-6}), iron orebody (BIF) (jt_{1-7}), and black–gray phyllite (jt_{1-8}) from base to top (Fig. 3).

The orebodies are stratiform and stratoid (Fig. 4a), with a conformable contact against the wall rocks (Fig. 4b), and fault contact locally. Three distinctive sedimentary facies are recognized in the JBIF on the basis of predominant iron minerals within the iron-rich layers: (1) oxide facies, composed of specularite (hematite) and jasper; (2) carbonate facies, in which the most prominent carbonate minerals are siderite and ankerite; (3) mixed carbonate-oxide facies, containing varying specularite and carbonate minerals. The JBIF strikes NW to SE with no significant sedimentary facies varying. Vertically, oxide facies BIFs are usually distributed at the upper and middle parts of the iron orebodies. Carbonate facies BIFs are mainly distributed at the middle and lower parts of the iron orebodies. In addition, mixed carbonate-oxide facies
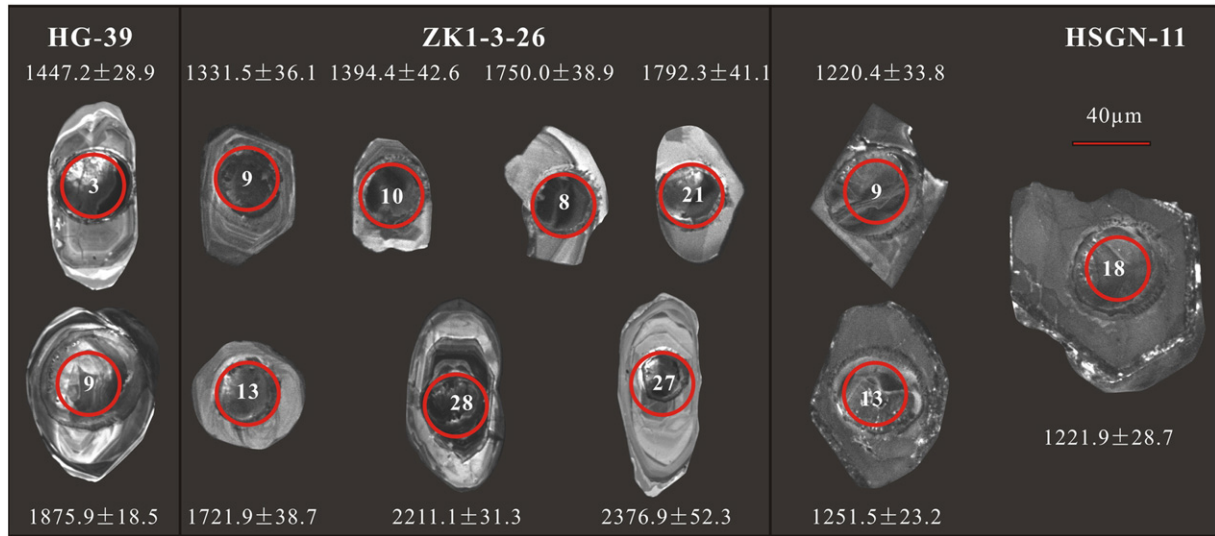
Fig. 5. CL images of zircon grains in metasedimentary rocks (HG-39 and ZK1-3-26) and diabase sample (HSGN-11). The circles are analysis spots marked with ages (Ma).

BIFs are the dominant sedimentary facies, and they were found in the upper, middle and lower parts of the iron orebodies. Barite is usually closely associated with BIF, with barite-rich band or finely granular in iron ore. Discrete, lenticular and stratiform barite orebodies also occur at the top of the iron orebodies. The barite, as well as BIF, are of sedimentary-exhalative origin (SEDEX) (Xue et al., 1997; Mao et al., 2003; Yang et al., 2015), and precipitated in association with submarine hydrothermal activity, but far away from the hydrothermal vents (Yang et al., 2015). We considered that the JBIF represents a unique type of BIF (Yang et al., 2015), in contrast to the common Algoma-, Superior- (Gross, 1965; Gross and McLeod, 1980), and Rapitan-types (Button et al., 1982; James, 1992).

Diabase dykes (Figs. 3, 4c and d) and quartz dioritic–porphyrite dykes (Fig. 3) are common within the Jingtieshan area. Recent zircon LA-ICP-MS U–Pb data indicate that quartz dioritic–porphyrite intruded in the Caledonian (421–476 Ma) (Zhao et al., 2003a; Zhang et al., 2008). However, all of the diabase dykes have not yet been dated.

3. Sampling and analytical procedures

3.1. Sampling

Two phyllite (HG-39 and ZK1-3-26) samples and two diabase (JTS-G-3 and HSGN-11) samples were collected from the Jingtieshan deposit of the Jingtieshan Group. The sampling locations are shown in Fig. 3, and a detailed description is given below.

Both phyllite samples were collected from the interlayers of the Jingtieshan iron orebody. Sample HG-39 (black–gray phyllite, jt_{1-8}, Fig. 4e) was obtained from the Heigou mine. Sample ZK1-3-26 (gray–green phyllite, jt_{1-6}, Fig. 4f) was collected from a drill hole in the Huashugou mine. Both samples show phyllitic structure and fine-grained texture, and are mainly composed of sericite, quartz, and minor specularite, together with chlorite and zircon, and sample HG-39 is characterized by higher amounts of specularite relative to sample ZK1-3-26 (Fig. 4h and i).

The diabase dykes intrude the meta-clastic-carbonate sedimentary formation (Jingtieshan Group) along the layer of the strata. The diabase samples analyzed in this study form parts of a series of dykes and intruded along the layer of calcareous phyllite (jt_{1-5}) (Figs. 3, 4c and d). The rock that is dark-green in color displays massive structure (Fig. 4g) and sub-ophitic texture (Fig. 4j). The diabase samples show similar mineral compositions of plagioclase (35%–45%), edenite and pyroxene (45%–55%), chlorite (2%–4%) and minor opaque minerals (magnetite, pyrite and chalcopyrite) (Fig. 4j).

3.2. Analytical procedures

3.2.1. Dating methods

Zircon concentrates were separated by using standard density and magnetic separation techniques. Representative zircon grains were selected by hand-picking under a binocular microscope. The grains were mounted in an epoxy disk with the Temora zircon standard (417 Ma; Black et al., 2003) and polished to expose their centers. Internal structures of zircon grains were revealed by cathodoluminescence (CL-image). The U–Pb isotope and trace elements analysis of zircons were performed on Finnigan Neptune inductively MC-ICP-MS that connected to a Newwave UP-213 laser ablation at the isotopic laboratory of Institute of Mineral Resources, Chinese Academy of Geological Sciences. The laser beam is with a spot diameter of 25 μm, frequency of 10 Hz and energy density of about 2.5 J/cm². Zircon TEM was used as external standard to correct instrumental mass discrimination and elemental fractionation. Zircon GJ-1 was treated as quality control for geochronology. Following the operating processes and calculation described in detail by Hou et al. (2009). Analyses in the data table and Concordia plots are reported at the 1σ level, and uncertainties in the weighted mean ages are quoted at the 95% confidence level. U–Pb ages are mentioned as $^{207}Pb/^{206}Pb$ ages.

3.2.2. Whole-rock geochemical analyses

After screening under the microscope, relatively fresh samples were selected, crushed, and powdered in an agate mill to 200 meshes. Whole-rock major and trace element (include rare earth elements) analyses were carried out at the State Key Laboratory of Geological Process and Mineral Resources, China University of Geoscience, Beijing. Major elements were analyzed suing fused glass disks with a scanning wavelength dispersion X-ray fluorescence (XRF) spectrometer. Trace element compositions were determined using an Agilent 7500a inductively coupled plasma mass spectrometer (ICP-MS) after acid digestion of samples in Teflon bombs. The precision of trace element data is better than 5% RSD with comparable accuracies.

4. Analytical results

4.1. Zircon U–Pb dating

4.1.1. Sample HG-39

Only few small detrital zircon were separated from this sample with grain size mostly less than 100 μm. The grains range in shapes from

Table 1
U–Pb data for zircons from metasedimentary rocks and diabase samples in the Jingtieshan area, North Qilian.

Spots	Concentrations (ppm)			Th/U	207Pb/206Pb		207Pb/235U		206Pb/238U		207Pb/206Pb		207Pb/235U		206Pb/238U		Concordance
	Pb_rad	232Th	238U		Ratio	1σ	Ratio	1σ	Ratio	1σ	Age (Ma)	1σ	Age (Ma)	1σ	Age (Ma)	1σ	
Phyllite sample (HG-39)																	
1	169.19	297.15	699.87	0.42	0.09263	0.00175	2.72817	0.04699	0.21316	0.00239	1480.6	36.3	1336.2	12.8	1245.6	12.7	92%
2	133.90	159.35	385.06	0.41	0.10345	0.00115	4.38009	0.06154	0.30631	0.00300	1686.7	20.4	1708.6	11.6	1722.5	14.8	99%
3	237.95	578.90	866.85	0.67	0.09103	0.00139	2.84510	0.04196	0.22632	0.00228	1447.2	28.9	1367.5	11.1	1315.2	12.0	96%
4	92.22	89.85	199.90	0.45	0.13606	0.00409	7.03886	0.21158	0.37447	0.00502	2177.5	52.2	2116.4	26.7	2050.4	23.5	96%
5	133.18	248.84	327.24	0.76	0.11454	0.00337	5.04613	0.11761	0.32166	0.00963	1872.5	52.3	1827.1	19.8	1797.8	47.0	98%
6	116.70	218.10	278.76	0.78	0.12739	0.00346	6.08057	0.16146	0.34552	0.00654	2062.0	48.2	1987.5	23.2	1913.2	31.3	96%
7	153.68	294.83	415.95	0.71	0.12252	0.00249	4.92646	0.10880	0.29098	0.00543	1994.4	31.3	1806.8	18.6	1646.4	27.1	90%
8	172.02	264.99	310.01	0.85	0.14858	0.00268	8.81197	0.16211	0.42888	0.00378	2329.3	31.3	2318.7	16.8	2300.7	17.0	99%
9	145.38	79.05	438.46	0.18	0.11467	0.00116	4.84849	0.05639	0.30614	0.00282	1875.9	18.5	1793.4	9.8	1721.7	13.9	95%
10	64.83	158.05	280.46	0.56	0.09158	0.00145	2.46866	0.03941	0.19555	0.00194	1459.0	29.9	1262.9	11.5	1151.4	10.5	90%
11	115.44	374.81	303.78	1.23	0.12349	0.00208	5.07519	0.17987	0.29777	0.00991	2007.1	29.9	1832.0	30.1	1680.2	49.2	91%
Phyllite sample (ZK1-3-26)																	
1	108.96	275.01	405.24	0.68	0.09648	0.00605	2.83706	0.13208	0.22071	0.01221	1566.7	117.4	1365.4	35.0	1285.6	64.5	93%
2	123.42	263.67	487.16	0.54	0.10536	0.00298	3.21830	0.09315	0.22108	0.00325	1720.7	47.2	1461.6	22.4	1287.6	17.1	87%
3	187.83	323.16	566.82	0.57	0.10845	0.00244	4.27654	0.09017	0.28627	0.00302	1773.8	41.0	1688.9	17.4	1622.9	15.1	96%
4	346.09	351.82	758.24	0.46	0.16066	0.00710	8.67088	0.29319	0.39297	0.00841	2462.7	74.2	2304.0	30.8	2136.6	38.9	92%
5	53.08	161.84	204.10	0.79	0.09681	0.00406	2.87297	0.12895	0.21382	0.00391	1564.8	78.5	1374.9	33.8	1249.1	20.8	90%
6	93.54	327.50	230.55	1.42	0.12036	0.00292	5.29535	0.12015	0.32781	0.01297	1961.4	44.0	1868.1	19.4	1827.7	63.0	97%
7	66.71	35.25	172.55	0.20	0.11022	0.00482	5.59224	0.27725	0.36505	0.00873	1803.4	79.6	1914.9	42.7	2006.1	41.3	95%
8	109.60	140.97	296.21	0.48	0.10701	0.00227	4.91514	0.10056	0.33183	0.00341	1750.0	38.9	1804.9	17.3	1847.3	16.5	97%
9	209.48	400.98	687.89	0.58	0.08568	0.00177	3.17010	0.06395	0.26763	0.00317	1331.5	36.1	1449.9	15.6	1528.8	16.1	94%
10	153.91	795.15	453.37	1.75	0.08853	0.00197	2.86495	0.06655	0.23360	0.00279	1394.4	42.6	1372.7	17.5	1353.4	14.6	98%
11	106.31	86.65	139.08	0.62	0.21185	0.00433	17.88943	0.41747	0.61704	0.01328	2919.4	33.8	2983.8	22.4	3098.1	52.9	96%
12	105.45	109.69	280.95	0.39	0.10374	0.00220	4.85996	0.14173	0.34078	0.00848	1692.3	38.9	1795.3	24.6	1890.4	40.8	94%
13	105.64	105.23	307.08	0.34	0.10543	0.00218	4.54053	0.12300	0.31329	0.00699	1721.9	38.7	1738.4	22.5	1756.9	34.3	98%
14	54.92	121.83	209.53	0.58	0.09143	0.00239	2.81947	0.09665	0.22695	0.00704	1455.3	50.0	1360.7	25.7	1318.5	37.0	96%
15	73.21	111.76	114.78	0.97	0.17419	0.00392	11.52949	0.34580	0.48269	0.01265	2598.5	37.7	2567.0	28.0	2539.0	55.0	98%
16	122.91	103.03	353.32	0.29	0.11229	0.00233	4.93295	0.13673	0.31925	0.00746	1836.7	37.7	1807.9	23.4	1786.1	36.4	98%
17	177.42	299.68	586.65	0.51	0.10429	0.00198	3.77262	0.11529	0.26410	0.00769	1702.2	34.9	1586.9	24.5	1510.8	39.2	95%
18	125.36	167.80	280.04	0.60	0.12722	0.00282	6.34562	0.16089	0.36498	0.00812	2061.1	39.2	2024.8	22.2	2005.7	38.3	99%
19	112.33	116.35	299.04	0.39	0.10624	0.00209	4.95880	0.14244	0.34132	0.00948	1736.1	36.6	1812.3	24.3	1893.0	45.5	95%
20	96.22	142.05	345.35	0.41	0.10939	0.00217	3.61340	0.09639	0.24109	0.00572	1790.7	35.6	1552.5	21.2	1392.4	29.7	89%
21	72.48	76.88	201.00	0.38	0.10956	0.00248	4.93016	0.13788	0.32958	0.00790	1792.3	41.1	1807.5	23.6	1836.3	38.3	98%
22	123.72	78.98	204.67	0.39	0.19327	0.00373	13.28872	0.27779	0.49939	0.00878	2770.1	31.8	2700.4	19.7	2611.2	37.8	96%
23	65.14	121.02	224.14	0.54	0.09739	0.00216	3.37628	0.08230	0.25185	0.00398	1575.9	42.1	1498.9	19.1	1448.0	20.5	96%
24	112.22	150.76	357.99	0.42	0.10698	0.00161	4.21092	0.08206	0.28367	0.00351	1750.0	27.8	1676.1	16.0	1609.8	17.6	95%
25	46.00	53.72	137.92	0.39	0.11775	0.00238	4.94453	0.13864	0.30346	0.00595	1924.1	35.6	1809.9	23.7	1708.4	29.4	94%
26	63.65	325.58	172.36	1.89	0.09370	0.00296	3.07519	0.13309	0.23991	0.00853	1502.2	59.3	1426.5	33.2	1386.2	44.4	97%
27	281.69	312.92	640.66	0.49	0.15275	0.00471	7.60822	0.20868	0.36016	0.00782	2376.9	52.3	2185.8	24.6	1982.9	37.1	90%
28	125.38	117.36	257.14	0.46	0.13783	0.00244	8.31291	0.17761	0.43693	0.00695	2211.1	31.3	2265.7	19.4	2336.9	31.2	96%
Diabase sample (JTS-G-3)																	
1	2525.96	292.43	211.43	1.38	0.08139	0.00044	2.06085	0.02340	0.18355	0.00161	1231.5	11.1	1135.9	7.8	1086.3	8.8	95%
2	3719.83	415.61	302.52	1.37	0.08163	0.00033	2.07844	0.01253	0.18467	0.00102	1236.7	13.4	1141.7	4.1	1092.4	5.5	95%
3	4036.82	413.00	320.12	1.29	0.08177	0.00022	2.22451	0.01049	0.19730	0.00085	1239.8	10.2	1188.8	3.3	1160.8	4.6	97%
4	3392.81	332.16	290.30	1.14	0.08110	0.00021	2.21693	0.01077	0.19828	0.00091	1233.3	4.2	1186.4	3.4	1166.1	4.9	98%
5	903.57	107.59	63.87	1.68	0.08110	0.00086	2.17814	0.04831	0.19477	0.00379	1233.3	26.1	1174.1	15.4	1147.2	20.4	97%
6	3376.37	350.58	285.87	1.23	0.08104	0.00020	2.21234	0.00983	0.19802	0.00082	1233.3	5.1	1185.0	3.1	1164.7	4.4	98%
7	1663.37	184.33	149.99	1.23	0.08162	0.00142	2.26900	0.04216	0.20176	0.00204	1236.1	1.7	1202.7	13.1	1184.8	10.9	98%
8	2751.20	294.89	229.18	1.29	0.08167	0.00209	2.30774	0.07075	0.20442	0.00137	1238.9	50.0	1214.7	21.7	1199.0	7.3	98%
9	3706.54	456.99	304.40	1.50	0.08166	0.00026	2.14738	0.01408	0.19062	0.00097	1238.9	6.0	1164.2	4.5	1124.7	5.2	96%
10	4105.59	442.04	260.01	1.70	0.08183	0.00028	2.38572	0.01940	0.21147	0.00162	1242.6	6.3	1238.3	5.8	1236.6	8.6	99%
Diabase sample (HSGN-11)																	
1	198.54	974.47	895.61	1.09	0.08234	0.00111	1.84144	0.02533	0.16151	0.00137	1253.7	25.9	1060.4	9.1	965.1	7.6	90%
2	257.65	1369.17	1000.30	1.37	0.08125	0.00149	2.00678	0.04257	0.17767	0.00247	1227.8	37.0	1117.8	14.4	1054.2	13.5	94%
3	274.74	1365.43	1087.13	1.26	0.08168	0.00135	2.10609	0.03947	0.18569	0.00253	1238.9	32.2	1150.8	12.9	1098.0	13.7	95%
4	406.69	2238.32	1725.51	1.30	0.08138	0.00131	1.86046	0.04294	0.16382	0.00308	1231.5	31.9	1067.1	15.2	978.0	17.0	91%
5	280.95	1606.99	1096.74	1.47	0.08239	0.00186	2.00506	0.04636	0.17463	0.00297	1254.6	44.0	1117.2	15.7	1037.5	16.3	92%
6	401.75	1714.38	1462.30	1.17	0.08207	0.00290	2.25524	0.14050	0.19741	0.01148	1247.2	69.3	1198.4	43.9	1161.4	61.8	96%
7	380.75	2008.31	1547.08	1.30	0.08032	0.00198	1.91153	0.06478	0.17052	0.00308	1205.6	49.2	1085.1	22.6	1015.0	17.0	93%
8	334.52	1711.64	1439.44	1.19	0.08080	0.00159	1.88533	0.04395	0.16752	0.00285	1216.7	38.9	1075.9	15.5	998.5	15.7	92%
9	220.47	1020.94	841.05	1.21	0.08097	0.00140	2.13479	0.04492	0.18980	0.00246	1220.4	33.8	1160.1	14.6	1120.3	13.3	96%
10	233.89	1068.95	1011.29	1.06	0.08019	0.00311	1.96687	0.08813	0.17791	0.00546	1266.7	75.9	1104.2	30.2	1055.6	29.9	95%
11	500.40	2415.10	1725.08	1.40	0.08363	0.00117	2.36464	0.03466	0.20471	0.00219	1284.3	26.7	1232.0	10.5	1200.5	11.7	97%
12	308.74	1502.22	1276.11	1.18	0.08137	0.00207	2.01371	0.04863	0.17992	0.00434	1231.5	45.4	1120.1	16.4	1066.6	23.7	95%
13	273.82	1282.50	1131.06	1.13	0.08225	0.00112	2.09214	0.02808	0.18409	0.00124	1251.5	23.2	1146.2	9.2	1089.3	6.8	94%
14	350.64	1642.37	1408.07	1.17	0.08008	0.00186	2.09637	0.04538	0.18940	0.00175	1199.1	45.2	1147.6	14.9	1118.1	9.5	97%
15	345.51	1559.14	1241.10	1.26	0.08283	0.00119	2.38335	0.03300	0.20834	0.00143	1264.8	28.9	1237.9	9.9	1220.0	7.6	98%
16	324.33	1405.97	1222.12	1.15	0.08014	0.00106	2.25697	0.02993	0.20410	0.00159	1266.7	27.0	1199.0	9.3	1197.3	8.5	99%
17	471.63	2223.30	1526.56	1.46	0.08136	0.00120	2.51040	0.04369	0.22331	0.00199	1231.5	3.9	1275.0	12.6	1299.4	10.5	98%
18	244.53	1207.32	988.12	1.22	0.08101	0.00102	2.13007	0.02957	0.19042	0.00140	1221.9	28.7	1158.6	9.6	1123.6	7.6	96%
19	437.87	2196.62	1591.82	1.38	0.08079	0.00191	2.26326	0.05899	0.20297	0.00386	1216.7	46.8	1200.9	18.4	1191.2	20.7	99%

Pb_rad indicates the radiogenic portions. Most spots have discordance of <10%, except for spots 2 and 20 of sample ZK1-3-26.

Fig. 6. U–Pb concordia diagrams for zircons in the metasedimentary rock samples.

subequant to prismatic with the smaller grains exhibiting elongation ratios of less than 2:1. In the CL images, some zircon grains show oscillatory zoning (Fig. 5). Eleven U–Pb ages with a smaller error and a discordance of <10% are listed in Table 1 and plotted on a concordia diagram in Fig. 6a. The ages range from 1447 to 2339 Ma.

4.1.2. Sample ZK1-3-26

Most zircon crystals from this sample are subhedral, elongated and slightly rounded, and show oscillatory zoning in the CL images. Their size ranges widely from 50 to 150 μm, with the majority around ca. 80 μm (Fig. 5). Twenty eight ages were obtained which range from 1331 to 2919 Ma (Table 1 and Fig. 6b). Most of these are early Mesoproterozoic in age, among which 10 spots with ages between 1702 and 1803 Ma, and yield a weight mean $^{207}Pb/^{206}Pb$ age of 1750 ± 24 Ma (MSWD = 0.68, n = 10) which is similar to the upper intercept age of the sample (1759 ± 31 Ma, MSWD = 3.5) (Fig. 7b).

4.1.3. Sample JTS-G-3

Zircon crystals from this sample are short prismatic in shape, with 50–150 μm in length and length to width ratio of 1:1 to 3:1. Ten analyses of ten zircon grains were obtained, and show U and Th contents and Th/U ratios are 107.59–456.99 ppm, 63.87–320.12 ppm and 1.14–1.70, respectively. The high Th/U ratios suggest a magmatic origin (Hoskin and Schaltegger, 2003). The $^{207}Pb/^{206}Pb$ ages obtained from ten analytical spots are in the range 1232–1243 Ma (Table 1), and the data yield a weighted mean $^{207}Pb/^{206}Pb$ age of 1236 ± 3 Ma (n = 10, MSWD = 0.26), which is similar to the upper intercept age 1237 ± 12 Ma (MSWD = 4.4) (Fig. 7a).

4.1.4. Sample HSGN-11

Zircons from this sample typically occur as thin and platy crystals, between 60 and 150 μm in length, with length to width ratios ranging from 1:1 to 1:2. The grains do not show clear oscillatory zones (Fig. 5). They have relatively high Th and U contents with a range of 974.47–2415.10 ppm and 841.05–1725.51 ppm, respectively. The Th/U values range from 0.65 to 1.83. The total rare earth element contents of the zircon range from 3968.00 to 9624.32 ppm (Table 2). The chondrite normalized patterns for all zircons exhibit HREE enrichment, distinctly positive Ce anomalies and negative Eu anomalies (Fig. 8), together with the high Th/U ratios and limited variation age range, which are typical of magmatic origin (Hoskin, 2005). A total of 19 analyses were carried out on 19 zircon grains, and the results show $^{207}Pb/^{206}Pb$ ages ranging from 1199 Ma to 1284 Ma (Table 1). All the analyses define a weighted mean $^{207}Pb/^{206}Pb$ age of 1234 ± 7 Ma (n = 19, MSWD = 0.55), which is similar to the upper intercept age (1243 ± 21 Ma, MSWD = 2.6) (Fig. 8b).

Although zircons are rare in the silica-unsaturated rocks such as diabase, it is still possible to obtain syn-magmatic zircons from these rocks which record yield reliable ages (e.g., Wingate et al., 1998), like zircons from diabase in Jingtieshan area with magmatic origin as discussed above. Hence, we conclude that the diabase dykes within the Mesoproterozoic sedimentary strata (Jingtieshan Group) were emplaced at around 1.23 Ga.

4.2. Whole-rock major and trace elements

4.2.1. Metasedimentary rocks

The geochemical data of Jingtieshan Group metasedimentary rocks (four black–gray phyllite samples and five gray–green phyllite samples)
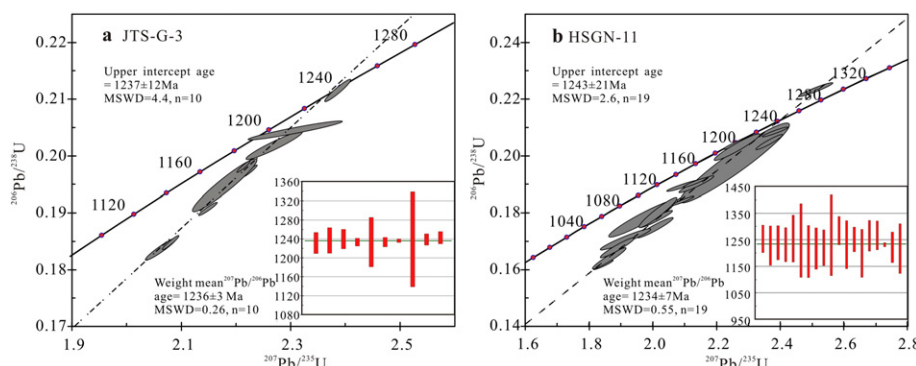
Fig. 7. U–Pb concordia diagrams for zircons in the diabase samples.

Table 2
Rare earth elements for zircons from diabase samples in the Jingtieshan area, North Qilian.

Spots	La	Ce	Pr	Nd	Sm	Eu	Gd	Tb	Dy	Ho	Er	Tm	Yb	Lu	REE	Ce/Ce*	Eu/Eu*
1	4.04	98.87	2.69	22.07	29.04	2.55	148.97	49.70	584.77	220.00	935.49	188.46	1619.73	306.49	4212.88	7.12	0.10
2	0.23	99.43	1.74	29.25	62.30	4.39	324.84	100.23	1090.60	369.46	1408.19	258.72	2074.69	356.23	6180.29	16.81	0.08
3	0.45	98.91	1.58	25.11	48.94	4.77	276.71	87.91	978.49	341.90	1356.64	254.11	2021.63	348.54	5845.68	17.48	0.10
4	5.56	222.77	4.43	53.23	84.94	7.44	432.66	134.41	1459.11	493.29	1899.50	351.21	2724.39	447.03	8319.97	10.38	0.10
5	3.34	80.86	1.95	28.61	58.98	4.42	340.86	110.63	1234.00	438.63	1766.17	334.25	2674.49	496.76	7573.95	7.63	0.07
6	0.33	94.17	1.78	30.38	51.55	6.45	295.25	87.60	979.32	321.80	1275.28	233.73	1827.29	301.05	5505.99	15.24	0.13
7	3.80	123.82	3.05	38.08	56.77	5.55	322.82	109.84	1221.14	449.60	1809.77	350.17	2835.58	511.50	7841.50	8.41	0.10
8	0.32	99.60	1.79	25.66	53.34	4.10	288.40	94.87	1076.47	374.76	1477.19	282.12	2283.61	387.99	6450.21	16.13	0.08
9	0.77	51.05	1.60	21.26	37.57	4.28	223.18	73.13	841.67	300.32	1198.18	225.19	1841.62	320.04	5139.85	8.33	0.11
10	0.14	58.96	1.18	18.17	36.74	2.79	203.67	68.94	796.47	286.59	1163.03	228.68	1914.31	335.91	5115.57	14.81	0.08
11	0.61	195.77	3.75	61.43	119.12	8.78	582.04	181.13	1891.74	599.99	2171.18	385.09	2964.98	458.73	9624.32	15.22	0.08
12	0.31	86.18	1.76	33.58	58.15	4.95	298.92	99.97	1089.67	363.62	1417.52	256.95	2054.33	330.25	6096.15	14.22	0.09
13	0.99	82.97	2.36	35.67	63.17	5.79	316.13	96.88	998.45	314.73	1156.83	207.05	1641.13	258.51	5180.65	9.34	0.10
14	0.22	97.53	2.18	35.05	58.32	6.86	295.03	89.65	953.75	299.12	1124.30	202.57	1580.92	246.33	4991.82	13.39	0.13
15	0.36	71.48	1.04	17.61	36.64	2.90	213.72	68.06	731.91	241.28	909.58	164.94	1300.71	207.77	3968.00	18.80	0.08
16	0.96	103.77	1.34	18.82	37.19	4.09	227.57	74.90	828.70	273.18	1043.71	189.43	1504.09	236.12	4543.85	18.68	0.10
17	0.37	161.96	2.73	45.99	88.14	8.64	443.89	133.61	1407.40	457.18	1701.70	307.35	2354.22	378.03	7491.20	17.47	0.11
18	0.21	63.60	1.07	16.24	33.25	3.49	198.10	64.99	761.53	276.13	1165.07	226.88	1929.68	357.26	5097.49	17.19	0.10
19	0.30	133.53	2.17	38.48	82.78	6.76	450.24	148.43	1673.75	528.93	2060.71	390.83	3078.35	503.22	9098.48	18.07	0.09

Note: $Eu/Eu^* = 2 * Eu_N/(Sm_N + Gd_N)$; $Ce/Ce^* = 2 * Ce_N/(La_N + Pr_N)$.
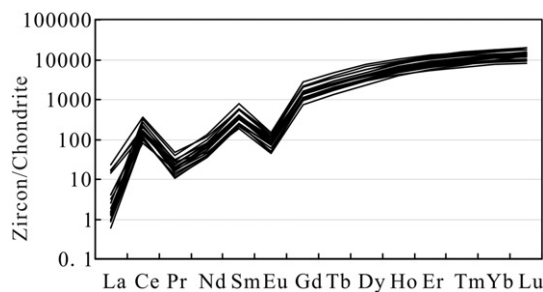
Fig. 8. REE patterns for zircons from diabase samples (normalization values are from Sun and McDonough (1989)).

are presented in Table 3. Both black–gray phyllite and gray–green phyllite samples show homogeneous composition, with SiO_2 and Al_2O_3 as the dominant components. The black–gray phyllite exhibits a narrow range of SiO_2 and Al_2O_3 contents in the range of 64.57%–67.93% and 10.35%–11.61% respectively. The rocks are enriched in K_2O (4.38%–4.92%) compared to Na_2O (0.04%–0.05%). The gray–green phyllite samples also display a narrow range of SiO_2 (61.59%–72.55%) and Al_2O_3 contents (9.66%–11.15%). K_2O and Na_2O contents are in the range of 4.03%–4.35% and 0.03%–0.06%, respectively. Based on the classification diagram of Herron (1988) (Fig. 9), the protoliths of the black–gray phyllite and gray–green phyllite are discriminated as graywacke and litharenite. When compared to the upper continental crust (UCC) and Post Archean Australian Shale (PAAS) (McLennan, 2001; Cullers, 1995), the rocks of the present study are also characterized by high contents of TFe_2O_3 and K_2O, with a strong depletion in mobile constituents like CaO and Na_2O. Some metasedimentary rock samples show relatively higher LOI values (Table 3), and may contribute to the presence of barite, as the higher concentrations of Ba in these samples (Table 3).

The rare earth element (REE) concentrations (157.92–205.78 ppm for black–gray phyllite and 83.33–111.27 ppm for gray–green phyllite samples) are comparable with those of the UCC and PAAS. All samples show enrichment in LREE patterns (Fig. 10a) [$(La/Yb)_N$ = 8.07–9.21 and $(La/Yb)_N$ = 8.06–11.03, respectively]. The black–gray phyllite samples show moderate negative Eu anomalies (Eu/Eu^* = 0.69–0.72), suggestive of feldspar decomposition. Gray–green phyllite samples, however, exhibit slight positive Eu anomalies (Eu/Eu^* = 1.02–1.25), implying the accumulation of feldspar (Table 3).

Most of the black–gray phyllite samples show slightly higher trace elements concentrations when compared to gray–green phyllite samples. Although samples are enriched in Rb, Ba, and Pb and depleted in Sr, the other trace elements are comparable with those of the UCC (Fig. 10b). Preferential accumulation of iron oxide minerals (e.g., hematite) likely occurs in the metasedimentary rocks due to the higher Ti concentrations (8090–9146 ppm for black–gray phyllite and 6686–11,226 ppm for gray–green phyllite, respectively) than that of the UCC. All samples also show elevated Sc and V contents compared to that of UCC and PAAS.

4.2.2. Diabase

The geochemical data of the diabase samples are presented in Table 4. All the diabase samples show high content of SiO_2 (51.55%–54.11%). The total alkalis (K_2O + Na_2O) range from 4.34% to 6.32% (K_2O/Na_2O = 1.29–2.21). Their Al_2O_3 content ranges between 11.51% and 14.58%, and TiO_2 between 1.36% and 1.55%. The rocks show LOI ranging from 1.59% to 3.43% due to the slight alteration, as shown in Fig. 4j. Immobile trace elements are useful to identify and classify volcanic rocks, which have been extensively altered (Winchester and Floyd, 1977) and employed in the following discussion. In the Zr/TiO_2–Nb/Y discrimination diagram (Fig. 11a), all the six diabase samples plot in the subalkaline basalt region. Together with plots in the SiO_2–TFe_2O_3/

Table 3
Major (wt.%) and trace element (ppm) compositions of the metasedimentary rocks in the Jingtieshan area, North Qilian.

Sample	HG-40	HG-41	HG-42	HG-43	ZK1-3-21	ZK1-3-22	ZK1-3-23	ZK1-3-24	ZK1-3-25
	Black–gray phyllite				Gray–green phyllite				
SiO_2	64.57	67.93	67.14	65.05	61.59	71.27	65.14	72.55	69.21
TiO_2	0.88	0.84	0.92	0.90	0.91	1.02	1.02	0.81	1.11
Al_2O_3	10.35	10.93	11.61	11.45	9.42	10.19	9.66	10.43	11.15
TFe_2O_3	8.97	9.04	9.40	9.16	8.88	6.32	9.67	5.60	6.76
MnO	0.45	0.08	0.04	0.25	0.13	0.08	0.06	0.07	0.07
MgO	2.53	2.41	2.36	2.18	2.57	1.92	2.02	1.27	2.15
CaO	1.92	0.50	0.35	1.25	2.52	0.33	0.34	0.35	0.28
Na_2O	0.05	0.05	0.04	0.05	0.04	0.03	0.04	0.04	0.06
K_2O	4.38	4.39	4.63	4.92	4.03	4.22	4.08	4.24	4.35
P_2O_5	0.14	0.11	0.13	0.14	0.03	0.02	0.03	0.02	0.02
LOl	4.90	2.78	2.49	3.82	9.04	4.12	7.02	3.96	3.87
CIA	68	69	69	68	68	69	68	69	69
PIA	97	98	98	98	98	98	98	98	97
Al_2O_3/TiO_2	12	13	13	13	10	10	9	13	10
Li	35.66	45.15	43.81	39.14	18.52	25.26	34.44	11.91	35.03
P	781.70	650.89	710.95	812.06	228.62	122.42	233.64	99.18	156.55
K	42,120	43,546	44,712	51,178	43,099	42,422	43,243	35,525	44,280
Sc	26.36	27.18	27.28	29.40	28.30	35.30	38.92	25.12	34.18
Ti	8216	8090	8658	9146	9478	9696	10,322	6686	11,226
V	162.14	161.00	164.02	200.60	174.04	224.00	217.60	140.70	233.80
Cr	93.18	92.84	95.28	109.20	184.62	217.20	215.20	135.78	212.20
Mn	4910	844	408	2930	1614	885	725	650	792
Co	34.36	36.78	35.62	35.52	45.14	34.52	21.90	7.14	25.12
Ni	60.48	72.98	68.48	77.10	46.10	38.82	81.66	35.12	48.50
Cu	11.92	8.56	7.30	5.69	214.00	720.60	134.26	24.56	62.94
Zn	267.80	343.80	351.40	239.20	45.90	52.94	42.70	37.90	72.16
Ga	23.62	24.14	24.90	28.82	24.58	24.40	24.16	20.10	26.42
Rb	190.82	191.18	197.72	227.00	188.32	188.70	175.66	149.08	194.20
Sr	32.68	8.18	5.45	24.54	90.60	13.96	11.68	32.26	14.55
Y	25.22	21.94	24.34	28.88	14.41	11.84	12.99	10.51	12.77
Zr	184.50	205.00	221.20	225.80	153.34	164.86	168.02	126.72	183.64
Nb	13.65	14.85	15.84	16.44	13.72	13.64	14.04	11.22	15.63
Cs	14.23	14.18	14.96	16.59	12.97	12.82	10.51	8.77	13.06
Ba	640.8	463.8	468.00	744.0	2280.0	1314.0	2880.0	3194.0	1249.4
La	29.44	30.92	30.74	38.40	21.74	16.22	19.01	20.76	17.36
Ce	69.28	68.64	69.64	91.54	49.58	36.88	43.92	49.82	37.54
Pr	7.97	7.85	7.96	10.12	5.17	3.93	4.64	5.32	3.96
Nd	30.64	28.58	29.50	37.00	18.54	14.17	16.68	19.23	13.88
Sm	6.01	5.01	5.13	6.71	3.84	2.67	3.33	3.80	2.61
Eu	1.34	1.08	1.13	1.53	1.42	0.89	1.31	1.42	0.85
Gd	5.56	4.38	4.68	6.07	3.58	2.32	3.09	2.97	2.35
Tb	0.87	0.69	0.74	0.93	0.52	0.36	0.47	0.40	0.38
Dy	4.85	4.10	4.43	5.34	2.85	2.17	2.81	2.25	2.33
Ho	0.97	0.85	0.93	1.09	0.56	0.46	0.57	0.45	0.50
Er	2.72	2.50	2.75	3.15	1.57	1.40	1.59	1.32	1.49
Tm	0.39	0.38	0.41	0.46	0.23	0.21	0.24	0.20	0.23
Yb	2.56	2.55	2.73	2.99	1.46	1.42	1.59	1.35	1.54
Lu	0.39	0.40	0.42	0.45	0.22	0.22	0.23	0.20	0.23
Hf	4.53	5.11	5.48	5.70	3.74	4.04	4.11	3.14	4.45
Ta	0.81	0.90	0.95	1.02	0.77	0.82	0.82	0.68	0.89
Pb	28.48	44.32	36.12	8.65	9.24	7.19	3.68	3.15	7.32
Th	8.63	9.34	9.47	10.34	6.34	5.75	5.95	6.18	7.14
U	1.53	1.53	1.57	1.60	1.14	1.19	1.37	0.88	1.31
REE	163.00	157.92	161.19	205.78	111.27	83.33	99.47	109.48	85.24
Eu/Eu*	0.70	0.69	0.69	0.72	1.15	1.07	1.22	1.25	1.02
$(La/Yb)_N$	8.24	8.70	8.07	9.21	10.69	8.20	8.56	11.03	8.06
Th/U	5.63	6.11	6.04	6.47	5.55	4.84	4.36	7.00	5.44

Note: TFe_2O_3 indicates total Fe; $Eu/Eu^* = 2 * Eu_N/(Sm_N + Gd_N)$; $(La/Yb)_N = La_N/Yb_N$.

MgO diagram (Fig. 11b), the diabases in the Jingtieshan iron deposit are classified as tholeiitic basalt.

All the diabase samples have relatively low total REE contents, varying from 76.74 ppm to 93.19 ppm (Table 4). In the chondrite-normalized REE diagrams (Fig. 12a), all the samples are characterized by slight LREE enrichment [$(La/Yb)_N = 2.43–3.12$], and lack distinct Eu ($Eu/Eu^* = 0.88–1.02$) and Ce anomalies ($Ce/Ce^* = 1.01–1.02$). In the primitive mantle-normalized spider diagram (Fig. 12b), all the diabase samples display a general enrichment in Rb, Ba, K, and Pb and depletion in Nb, Ta, and Sr.

5. Discussion

5.1. Age of JBIF and its implications

Previous geochronological studies were based on conventional whole rock Rb–Sr and Sm–Nd isotopic systems (Yang et al., 1991; Yang and Zhao, 1999) and the ages reported range from Neoproterozoic to Mesoproterozoic, largely resulting from strong hydrothermal alteration and isotopic resetting (e.g., Faure, 1977). The more robust U–Pb system and the high precision dating applied to zircon make our age
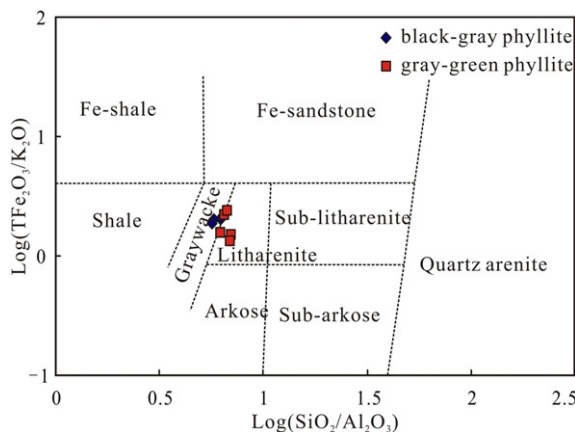
Fig. 9. Classification of sandstones using the major element composition (Herron, 1988).

data more reliable. The U–Pb data obtained on metasedimentary rocks and diabases from the Jingtieshan Group combined with field evidence allow us to evaluate the depositional age of the JBIF.

The youngest concordant zircon has an age of 1331.5 ± 36.1 Ma (Table 1), which might mark the maximum depositional age of the Jingtieshan Group. The zircon grains from diabase dykes within the Jingtieshan group show emplacement age of U–Pb age of 1234 ± 7 Ma and 1236 ± 3 Ma, which are interpreted as the minimum depositional age of Jingtieshan Group. Based on the U–Pb age constraints, we propose that the JBIF formed between 1.23–1.33 Ga, which is in agreement with Middle Mesoproterozoic (Ectasian) in age proposed by other workers (e.g., Yang and Zhao, 1999; Xia et al., 1999; Mao et al., 2003).

In the NQOB, many medium-scale and small-scale iron deposits like JBIF are hosted in the Mesoproterozoic Jingtieshan Group (Fig. 1), in contrast to most of the Archean BIFs in the NCC (Zhang et al., 2011; Wan et al., 2012; Zhang et al., 2012; Zhai and Santosh, 2013; Zhai, 2014; Li et al., 2014, 2015b) as well as Late Neoproterozoic BIFs in the SCB (Xu et al., 2014; Zhang et al., 2014). It is generally assumed that BIFs with ages between 1.8 and 0.8 Ga are absent on our planet (e.g., Isley and Abbott, 1999; Huston and Logan, 2004; Klein, 2005; Lascelles, 2014). Holland (1984, 2003) proposed that the absence of BIF during this period was due to the oxidation of the deep oceans. Canfield (1998) on the other hand, has suggested that most of the ferrous iron in the water column occurred as iron sulfide minerals as in the modern Black Sea, thus preventing BIF deposition. However, unlike the classic 'Canfield' euxinic ocean, newer data emphasizing details in C–S–Fe systematics (Planavsky et al., 2011; Poulton and Canfield, 2011), molybdenum isotope (Arnold et al., 2004), and molybdenum and chromium enrichments in Proterozoic sedimentary rocks (Reinhard et al., 2013), favor dominantly ferruginous conditions in the deep ocean through the mid-Proterozoic, much like the scenario during Archean. The large-scale JBIF in NQOB, those of Broken Hill (Richards, 1966; Lascelles, 2014) and Pecos greenstone belt in New Mexico

(Slack et al., 2009) with deposition age of 1.8–1.0 Ga, are direct evidence of at least episodic ferruginous oceanic conditions (Bekker et al., 2010; Poulton and Canfield, 2011).

5.2. Sedimentation and provenance

5.2.1. Provenance characteristics

Geochemical composition of terrigenous clastic rock has been widely utilized to decipher the composition of the source area (e.g. Roser and Korsch, 1988; McLennan et al., 1990; Nagarajan et al., 2014). Here we chose the metasedimentary rocks samples, whose protoliths are graywacke/litharenite (Fig. 9), to identify the provenance characteristics. The Chemical Index of Alteration (CIA) introduced by Nesbitt and Young (1982) is a robust measure to quantify the weathering degree of source rocks, and the CIA values are not significantly affected during metamorphism. The index is calculated using the expression: $CIA = [Al_2O_3/(Al_2O_3 + CaO^* + Na_2O + K_2O)]$. CaO^* represents the Ca present in the silicate fraction only, after correction for Ca containing in carbonate. We calculate CaO^* based on the method of Fedo et al. (1995) and Bock et al. (1998). The CIA values for all samples show a limit range, varying between 68 and 69. Studies have shown that low CIA values are recorded in fresh rocks, changing progressively to higher values in more intensely altered materials (Nesbitt and Young, 1982). The A–CN–K system is useful for evaluating fresh rock compositions and examining their weathering trend. In this diagram (Fig. 13), all sample plots along the A–K tie line and group around ~70% Al_2O_3 contents. In addition, the high K_2O contents found in both samples also reflect secondary addition of potassium (K-metasomatism) (Fedo et al., 1995). The Plagioclase Index of Alteration [$PIA = (Al_2O_3 + K_2O)/(Al_2O_3 + CaO^* + K_2O + Na_2O) \times 100$] is another parameter to quantify the degree of chemical weathering that precludes the influence of K-metasomatism (Fedo et al., 1995). This diagenetic process can lead to conversion of aluminous clay minerals (e.g. kaolinite) into illite or transformation of plagioclase into K-feldspar. All samples in this study display generally high PIA values (PIA = 97–98), which suggests that the rocks have undergone extreme chemical weathering. Th/U ratios for sedimentary rocks generally increase with increasing degrees of weathering due to the oxidation and loss of uranium (McLennan et al., 1995). The higher Th/U ratios (Th/U = 4.4–7.0), which are greater than that of UCC (3.8, Taylor and McLennan, 1985), also indicate intense weathering of their source. This is further corroborated by the fact that all of the samples show strong depletion in CaO, Na_2O and Sr when compared to UCC and PAAS.

REE, Zr, Hf, Th, Sc, Cr and Co are useful elements for provenance characterization because, being less soluble, they are relatively immobile (Taylor and McLennan, 1985; McLennan et al., 1990). These elements are more or less transported in the terrigenous component and therefore, reflect the chemistry of their source (e.g., Sifeta et al., 2005). The plots of Th/Sc versus Zr/Sc can reflect the sedimentary sorting and recycling (Fig. 14) (Mclennan et al., 1993; Asiedu et al., 2000). First-
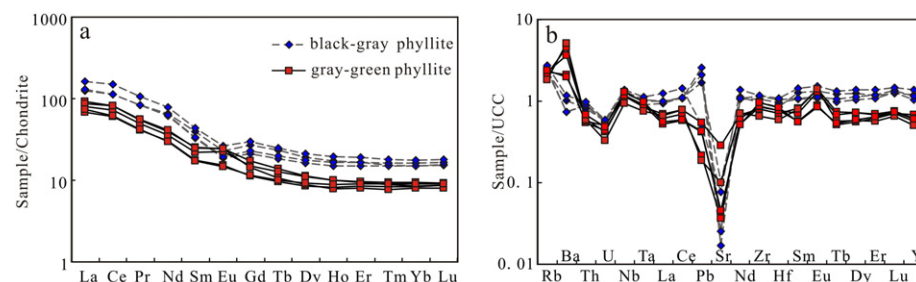
Fig. 10. Chondrite-normalized rare earth element diagrams and UCC normalized spidergrams for the metasedimentary rocks in the Jingtieshan iron deposit. Chondrite values are from Sun and McDonough (1989) and UCC values are from Rudnick and Gao (2003).

Table 4
Major (wt.%) and trace elements (ppm) compositions of the diabases in the Jingtieshan area, North Qilian.

Sample	HSGN-2	HSGN-3	HSGN-4	HSGN-5	HSGN-6	HSGN-7
SiO_2	51.55	53.20	54.11	52.44	52.00	53.36
TiO_2	1.53	1.37	1.55	1.42	1.36	1.46
Al_2O_3	11.51	14.58	11.81	13.24	13.03	12.67
TFe_2O_3	13.13	11.99	13.68	12.46	12.95	12.42
MnO	0.17	0.13	0.19	0.16	0.17	0.17
MgO	6.05	4.65	5.81	5.52	6.04	6.09
CaO	6.55	4.15	4.56	7.68	7.22	6.85
Na_2O	3.16	3.56	3.44	2.72	2.64	3.05
K_2O	2.07	2.76	1.61	1.63	1.73	1.38
P_2O_5	0.11	0.12	0.11	0.10	0.10	0.12
LOI	3.43	2.74	2.27	1.82	1.97	1.59
$Na_2O + K_2O$	5.23	6.32	5.05	4.34	4.37	4.43
Na_2O/K_2O	1.53	1.29	2.14	1.67	1.52	2.21
Li	76.7	110.9	64.72	72.07	31.11	29.81
P	798	918	791	729	481.8	541.2
K	17,936	27,065	13,906	14,222	10,617	8640
Sc	53.21	38.14	54.82	41.88	40.72	50.61
Ti	12,319	12,811	12,913	11,689	9430	10,907
V	503.5	624.3	561.6	497.7	421.0	444.6
Cr	304.81	239.44	7.48	20.53	17.18	227.69
Mn	1756	1538	2062	1691	1642	1797
Co	47.49	56.74	57.13	48.14	52.00	55.12
Ni	113.5	131.0	66.79	77.85	73.14	106.20
Cu	110.4	198.7	90.43	85.53	70.90	86.88
Zn	119.5	98.23	127.3	144.9	143.9	114.5
Ga	22.51	28.28	22.65	24.67	22.18	22.52
Rb	60.00	86.33	47.95	45.53	46.74	37.91
Sr	69.981	245.1	150.4	287.1	221.8	239.5
Y	29.81	27.22	31.89	25.00	26.46	32.45
Zr	104.8	102.5	111.7	93.5	87.4	99.6
Nb	8.236	7.724	8.416	7.136	7.144	8.761
Cs	2.859	3.500	2.794	1.489	1.807	1.363
Ba	306.1	510.1	364.2	333.8	298.4	245.8
La	11.89	13.54	13.02	11.29	11.08	12.71
Ce	27.58	30.30	29.96	25.47	25.36	29.43
Pr	3.683	3.930	3.983	3.338	3.328	3.899
Nd	15.90	16.52	17.12	14.19	14.19	16.71
Sm	4.240	4.166	4.557	3.675	3.728	4.489
Eu	1.348	1.512	1.472	1.343	1.293	1.447
Gd	5.182	4.909	5.516	4.391	4.422	5.345
Tb	0.918	0.844	0.987	0.773	0.761	0.927
Dy	5.855	5.293	6.285	4.914	4.826	5.915
Ho	1.278	1.155	1.386	1.079	1.045	1.273
Er	3.666	3.285	3.946	3.095	2.998	3.671
Tm	0.539	0.485	0.587	0.457	0.438	0.536
Yb	3.509	3.116	3.802	2.937	2.842	3.453
Lu	0.540	0.473	0.572	0.455	0.428	0.525
Hf	2.872	2.726	3.021	2.519	2.296	2.699
Ta	0.805	0.826	0.817	0.708	0.407	1.026
Pb	3.023	4.838	5.401	10.976	9.364	6.914
Th	3.580	3.828	4.063	3.343	2.654	3.056
U	0.949	1.044	1.272	1.176	0.687	0.699
ΣREE	86.13	89.53	93.19	77.41	76.74	90.34
$(La/Yb)_N$	2.43	3.12	2.46	2.76	2.80	2.64
Eu/Eu^*	0.88	1.02	0.90	1.02	0.97	0.90
Ce/Ce^*	1.01	1.01	1.01	1.01	1.01	1.02
Zr/Nb	12.72	13.27	13.27	13.11	12.23	11.36
Y/Nb	3.62	3.52	3.79	3.50	3.70	3.70

Note: TFe_2O_3 indicates total Fe; $Eu/Eu^* = 2*Eu_N/(Sm_N + Gd_N)$; $Ce/Ce^* = 2*Ce_N/(La_N + Pr_N)$; $(La/Yb)_N = La_N/Yb_N$.

cycle sediments show a simple positive correlation between Th/Sc and Zr/Sc, whereas additionally recycled sediments usually show a more rapid increase in Zr/Sc than in Th/Sc. In this study, all samples follow the general provenance-dependent compositional variation trend. It can, therefore, be inferred that the sediments were dominated by the erosion of intermediate igneous rocks in the source areas, and the samples are the products of proximal deposit without exhibiting a sedimentary recycle trend (Mclennan et al., 1993). The Al_2O_3/TiO_2 ratios vary in different source rocks, mechanical disintegration of these source rocks without significant weathering and incorporation of these debris leads to variable Al_2O_3/TiO_2 ratio in the resultant sediments (Hayashi et al.,

1997). The Al_2O_3/TiO_2 ratios range from 3 to 8 in mafic, 8 to 21 in intermediate and 21 to 70 in felsic igneous rocks and 15 to 25 in Precambrian sediments (Willis et al., 1988). Ratios of the black–gray phyllite samples in this study range from 12 to 13, whereas those of the gray–green phyllite samples range from 9 to 13, pointing to intermediate source rocks. Ratios such as Co/Th, La/Sc are very sensitive to the source rocks and can be ideal parameters in discriminating the source natures of sedimentary rocks. On a plot of Co/Th against La/Sc (Fig. 15a) the data are clustered around basalt and andesitic source composition. A plot of La/Th against Hf provides useful bulk rock discrimination between different source compositions (Floyd and Leveridge, 1987). In Fig. 15b, most
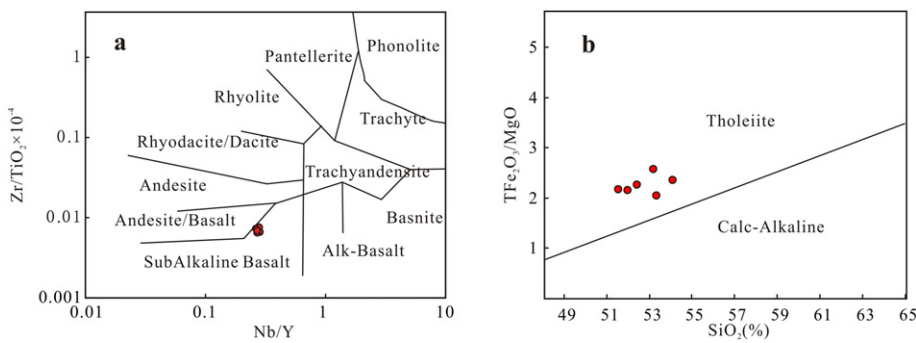
Fig. 11. Zr/TiO$_2$ versus Nb/Y plots (a) (after Meschede, 1986) and TFe$_2$O$_3$/MgO versus SiO$_2$ diagram (b) for diabase samples (after Irvine and Baragar, 1971) in the Jingtieshan iron deposit.
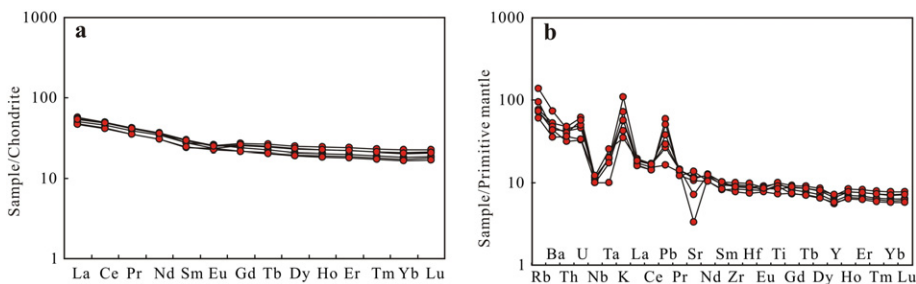
Fig. 12. Chondrite-normalized REE pattern (a) and primitive mantle-normalized spider diagram (b) of diabase samples in the Jingtieshan iron deposit. Chondrite values and primitive mantle values are from Sun and McDonough (1989).

samples plot in the mixed felsic and mafic sources suggesting that the sediments were derived from the erosion of basic and intermediate igneous rocks.

All the metasedimentary rocks in Jingtieshan area show geochemical characteristics of mafic and intermediate igneous rocks. These metasediments show high Sc and V contents compared to that of UCC and PAAS, indicating the presence of mafic components in the source, whereas the gray–green phyllite sample shows geochemical signatures of mafic igneous rocks. Mafic igneous rocks are typically characterized by low REE abundances and insignificant or nil negative Eu anomaly, whereas felsic rocks display higher REE contents and obvious negative Eu anomaly (Cullers et al., 1997). The black–gray phyllite samples show moderate to high REE abundances (157.92–205.78 ppm) and

obvious negative Eu anomalies (Eu/Eu* = 0.69–0.72) indicating that the parental rocks were possibly intermediate to felsic igneous rocks. In contrast, the gray–green phyllite samples show lower REE concentrations (83.33–111.27) and absence of negative Eu anomalies (Eu/Eu* = 1.02–1.25), suggesting derived predominantly from mafic sources. Most samples from gray–green phyllite plotted near basalt field on the Co/Th-La/Sc diagram (Fig. 15a) and show lower Al$_2$O$_3$/TiO$_2$ ratios, also supporting the above conclusion.

5.2.2. Sources of detrital zircons

Ages of detrital zircon populations are unaffected by fractionation processes within the sedimentary cycle and therefore provide a direct fingerprint for the identification and location of source terranes (Cawood and Nemchin, 2000). The U–Pb ages of zircons from the metasedimentary rocks in this study range from 1331 Ma to 2919 Ma. On the probability diagram (Fig. 16), the main age peaks are clustered around 1747 Ma and 1465 Ma, with only three grains showing Archean age. The distinct peak at 1747 Ma suggests rocks of this age as the
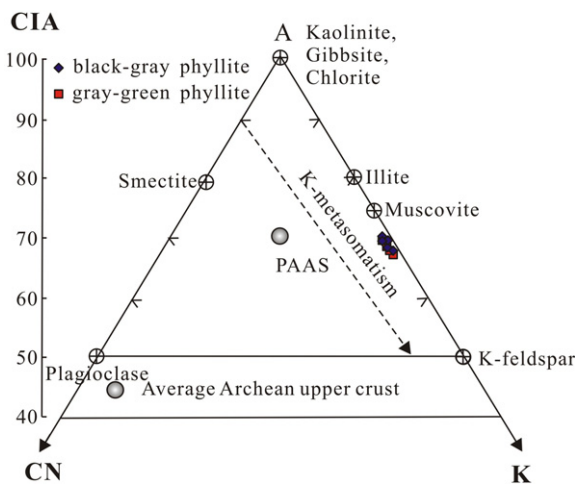
Fig. 13. Distribution of Al$_2$O$_3$, CaO* + Na$_2$O and K$_2$O of the metasedimentary rock samples in the A-CN-K ternary diagram of Nesbitt and Young (1982). The average composition of UCC and PAAS is considered from Taylor and McLennan (1985).
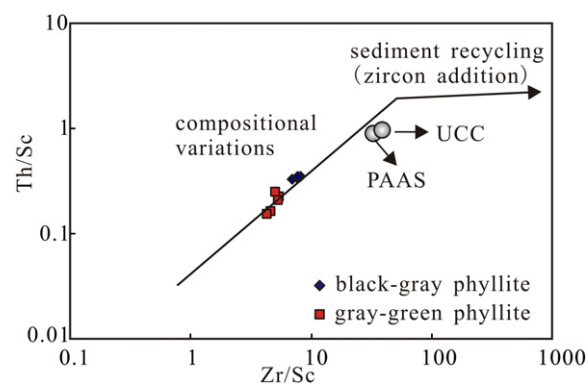
Fig. 14. Plot of Th/Sc versus Zr/Sc (after McLennan et al., 1993) for the metasedimentary rock samples in Jingtieshan iron deposit.
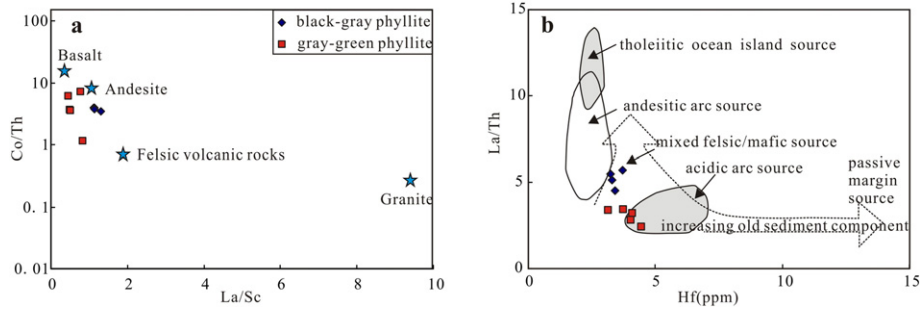
Fig. 15. Geochemical diagrams showing the source nature of the metasedimentary rocks in the Jingtieshan iron deposit. (a) La/Sc–Co/Th diagram after Gu et al. (2002). (b) La/Th–Hf diagram after Floyd and Leveridge (1987).

predominant source. This age is also similar to the weight mean ^{207}Pb/^{206}Pb age (1750 ± 24 Ma, MSWD = 0.68, n = 10) of 10 spots from sample ZK1-3-26 (Fig. 6b). Sources of the 1747 Ma zircons could come from magmatic rocks of the Zhulongguan Group (1.7–1.8 Ga), which unconformably lies beneath the Jingtieshan Group. The data also suggest that the depositional age of the Beidahe Group in NQOB is Paleoproterozoic, rather than <1400 Ma (Li et al., 2007; He et al., 2010). The provenance of detrital zircons of 1465 Ma is probably the granitic gneiss in the western segment of the NQOB (1463 Ma, Guo et al., 2002). The Caledonian quartz dioritic–porphyrite intrusive rocks in the Jingtieshan Group also contain inherited magmatic zircons with age of 1455 Ma (Zhang et al., 2008). This indicates that another important source of Jingtieshan Group is from rocks with age of 1465 Ma. There are three grains with Archean ages (2589 Ma, 2770 Ma and 2919 Ma), and similar Archean detrital zircon ages were also observed in the Beidahe Group (Li et al., 2007, 2013). The most obvious source of these zircons is the adjacent Dunhuang Block in the Tarim Craton, the Alxa block in NCC where Neoarchean TTG and supracrustal rocks are common (e.g., Che and Sun, 1996; Lu et al., 2008; Wang et al., 2013; Hu et al., 2014). The unexposed Archean basement in NQOB is another possible source.

In summary, various detrital zircon ages (1331–2919 Ma) of the metasedimentary rocks from the Jingtieshan Group suggest that the detrital zircons are derived from multiple sources. Zircons older than Neoarchean (2.5 Ga) were likely derived from the adjacent Dunhuang block in the Tarim Craton and NCC, whereas the majority of the zircon population is consistent with the tectono-thermal events in the North Qilian during the Early Mesoproterozoic. These were probably derived from the Zhulongguan Group in North Qilian. The detrital zircons of

mid-Mesoproterozoic were probably derived from the granitic gneiss in North Qilian.

5.3. Geotectonic implications

The NQOB at the southwestern margin of the NCC is considered to mark the suture zone that preserves a complete record of continental breakup, through ocean basin evolution, and to the final continental collision during Neoproterozoic to the Paleozoic (Song et al., 2013). However, the evolution history of NQOB during Paleoproterozoic–Mesoproterozoic is still not clear.

The chemical composition of sedimentary rocks is useful for determining the nature of their source region and tectonic setting (e.g., Bathia, 1983; Roser and Korsch, 1988). The metasedimentary rocks were subjected to intense K-metasomatism as mentioned previously. In this regard, trace elements such as REE, Zr, Th, Sc, Co and Y provide more reliable information for discriminating the tectonic setting. Plots shown in Fig. 17 suggest that these rocks were mainly sourced from basic to intermediate igneous rocks in an oceanic island arc and continental island arc. The Zhulongguan Group is suggested as the possible source, which is also confirmed by the detrital zircon ages. We consider that the geochemical characteristics of these rocks were inherited from the source. The basalt and andesite in the Zhulongguan Group shows characteristics of island arc (Zhang et al., 1998; Mao et al., 2003). The metasedimentary rocks in this study are terrigenous clastic rock sourced from the underlying Zhulongguan Group. Combining the thickness dolomitic marble on the upper lithostratigraphic units of Jingtieshan Group, we consider that the Jingtieshan Group deposited on continental marginal sea.

In most cases, high-field-strength elements (HFSE), rare earth elements (REE), Th and transition elements are immobile even during the most intense hydrothermal alteration (e.g. Hawkesworth et al., 1997), whereas Ca, Na, K, Al and some of the large ion lithophile elements (LILE; e.g. Sr, Ba and Rb) are considerably mobile (Smith, 1976). Thus, we exclude the mobile elements for petrogenetic interpretations. The 1.23 Ga diabases within the Jingtieshan Group in the Jingtieshan are classified as tholeiitic basalt. These diabase samples exhibit strong positive Rb, Ba, K, and Pb anomalies, negative Nb and Ta anomalies (Fig. 12b), and slight LREE-enrichment (Fig. 12a), suggesting that they underwent insignificant crustal contamination during magma evolution (McDonough and Sun, 1985). The negative Sr anomalies may be due to alteration (Wang et al., 2012). The trace element characteristics and REE patterns of the Jingtieshan diabase suggest a relatively deep source for the magma, possibly from the upper mantle (Ringwood, 1975). The diabase sample in the Jingtieshan area shows Zr/Nb ratios ranging from 11.36 to 13.27, which are lower than that of the average value of primitive mantle, and Y/Nb ratios ranging from 3.50 to 3.79, and La/Yb$_N$ ranging from 2.43 to 3.12, corresponding to those of the mafic rocks from the transitional mantle (LeRoex et al., 1983). This interpretation is further
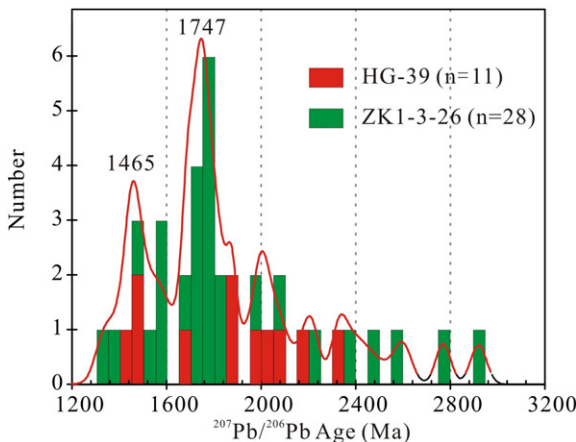
Fig. 16. Frequency histogram and probability curves of zircon ^{207}Pb/^{206}Pb ages for metasedimentary rock samples in Jingtieshan iron deposit.
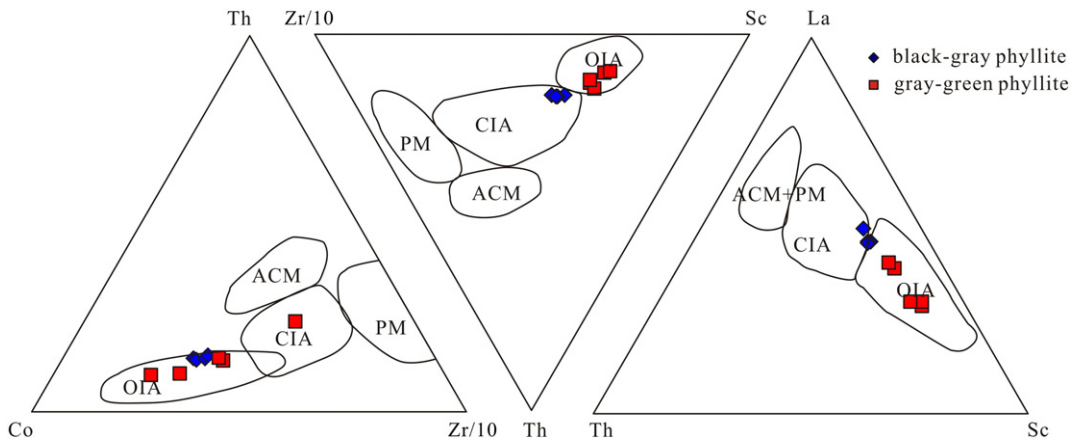
Fig. 17. Tectonic discrimination diagrams for metasedimentary rocks in the Jingtieshan iron deposit. Th–Sc–Zr/10 (a), Th–Sc–Zr/10 (b) and La–Th–Sc and (c) diagrams are after Bhatia and Crook (1986). OIA, oceanic island arc; CIA, continental island arc; PM, passive margin; ACM, active continental margin.
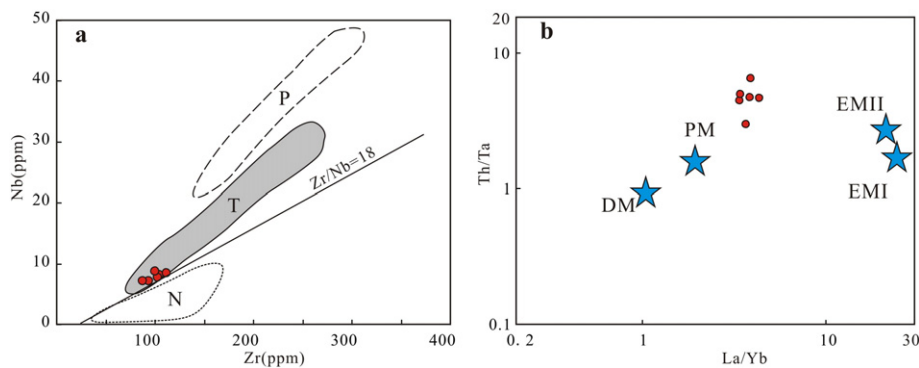

Fig. 18. (a) Plots of Zr vs. Y of the diabase samples in the Jingtieshan area. P: enriched mantle; N: depleted mantle; T: transitional mantle. Modified from LeRoex et al. (1983). (b) Plots of Th/Ta vs. La/Yb for the diabase samples from the Jingtieshan area. DM, depleted mantle; PM, ordinary mantle; EMI: enriched mantle type I; EMII, enriched mantle type II. Modified from Condie (1997).

supported by plots in the Zr–Nb diagram (Fig. 18a) and Th/Ta–La/Yb diagram (Fig. 18b).

Ti, Zr, Y and Nb are usually immobile, and thus can be used in many cases to identify the original tectonic settings of basic volcanic rocks (Pearce and Cann, 1973; Pearce and Norry, 1979). Most basalts erupted in within-plate settings can be identified by their high Ti/Y and Zr/Y ratios (Pearce and Norry, 1979). In Zr/Y–Zr (Fig. 19a) and Ti–Zr–Y (Fig. 19b) diagrams, all the samples plot in the transition area of the within-plate basalt and MORB, which is consistent with the interpretation that Mesoproterozoic Jingtieshan Group rocks are deposited on a

continental margin (Yang et al., 1991; Zhou and Yue, 1999; Mao et al., 2003; Yang et al., 2015; reference therein). We therefore propose that the diabase formed in continental margin sea, and infer that North Qilian was in continental extensional environment at 1.23 Ga.

The presence of Archean zircons has been recorded from the NQOB (e.g., Mao et al., 2003; Li et al., 2007 and reference therein). Neoarchean metamorphic rocks are distributed in the adjacent Tarim Craton and NCC (e.g., Che and Sun, 1996; Lu et al., 2008; Wang et al., 2013; Hu et al., 2014), suggesting that all these terranes share the same Archean basement. In our study, the age spectra of the detrital zircons from the
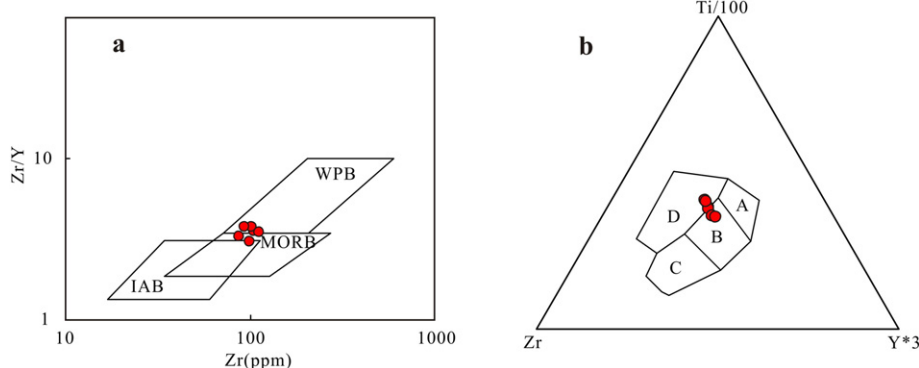
Fig. 19. Tectonic discrimination diagrams of Zr versus Zr/Y for diabase samples in the Jingtieshan area (Pearce and Norry, 1979). WPB—within plate basalts; MORB—mid ocean ridge basalts; IAB—island arc basalts. (b) Tectonic discrimination diagrams of Ti–Zr–Y for diabase samples in the Jingtieshan area (after Pearce and Cann, 1973). A—island-arc tholeiite; B—mid-ocean ridge, island-arc and calc-alkaline basalts; C—calc-alkaline basalts; D—within plate basalts.

two analyzed samples are mainly clustered between 1747 Ma and 1465 Ma (Fig. 16), indicating that the NQOB probably had undergone multiple tectono-thermal events during the Proterozoic era. The age peak of 1747 Ma for the detrital zircons from the Jingtieshan Group broadly coincides with the ages of the zircons in the igneous rocks of the NQOB, such as the rift-related basic dyke swarm of the Zhulongguan Group (e.g., Xu et al., 1996; Zhang et al., 1998; Xia et al., 1999). Furthermore, the metasedimentary rocks analyzed in this study are located at the western part of the NQOB, and the protolith rocks of these sediments were derived from the intermediate-basic volcanic rocks with typical oceanic island arc affinity belonging to the Zhulongguan Group.

The Paleo-Mesoproterozoic (1.8–1.2 Ga) marks the time of growth and breakup of the Columbia (Nuna) supercontinent (Zhao et al., 2002, 2003b, 2004; Rogers and Santosh, 2002, 2009; Meert, 2014; Nance et al., 2014). The NQOB experienced Paleoproterozoic continental rifting around ~1.75 Ga (e.g., Xu et al., 1996; Zhang et al., 1998), coeval with the time of the breakup of the Paleoproterozoic supercontinent Columbia. The deposition age of Jingtieshan Group is younger by 0.45 Ga than the underlying Zhulongguan Group (~1.75 Ga), indicating a long sedimentary hiatus between the two Groups (Fig. 2). The final breakup of Columbia supercontinent took place during 1.2–1.3 Ga (Zhao et al., 2002, 2004; Zhang et al., 2009; Wang et al., 2015). The 1.23 Ga diabase dykes reported in this study, which formed in continental extensional environment, are regarded as the products of the final breakup of the Columbia supercontinent. Mafic dyke swarms/sills of 1.4–1.3 Ga are widely distributed in North America, Greenland, Siberia, Baltica, Antarctica, Australia and the NCC (Ernst et al., 2008), whereas the mafic dyke swarms (mainly hosted in Zhulongguan Group) are mainly of ~1.75 Ga in age, suggesting the imprint of early rifting event of Columbia within the NQOB.

In summary, the 1.23 Ga diabase dykes formed not much younger than Jingtieshan Group, and we consider that the continental extensional environment where diabase formed also apply to the formation of the BIF in Jingtieshan area. Therefore, we conclude that the JBIF was deposited within continental margin sea in an extensional setting, likely a rift-basin which is related to the final breakup of the Columbia supercontinent. Many Neoproterozoic BIFs have been correlated to the Rodinia break-up (Xu et al., 2014; Basta et al., 2011), and occur in basins within the Rodinia fragments or in rift-basins developed at their margins (Cox et al., 2013). Processes including continental rifting events that led to the formation of dyke swarms and submarine mafic volcanic rocks, and enhanced spreading rates of mid ocean ridges, resulted in a higher rate of hydrothermal fluids flux to the ocean. Modern mid-ocean ridge hydrothermal systems typically release vent fluids to the ocean with dissolved H_2S in excess of Fe, causing the precipitation of FeS and FeS_2 (Kump and Seyfried, 2005). Under anoxic oceanic conditions, however, the role of hydrothermal dissolved-Fe(II) sources is much more significant, like in the case of rocks older than ~1.8 Ga, with Fe in excess of H_2S. Therefore, sufficient reduced iron released by submarine hydrothermal fluids is essentially stable in the bottom water conditions (Kump and Seyfried, 2005; Poulton and Canfield, 2011), which would have promoted the establishment of an iron-rich deep ocean in Jingtieshan area as we discussed above. Iron could be transported by upwelling currents onto the oxidizing shallow sea, resulted in the formation of JBIF (Yang et al., 2015). However, because of the lack of reliable ages for Meso-Neoproterozoic thermo-tectonic records in the NQOB, and the geological setting and nature of Precambrian basement is not clear, the detail relation between JBIF and the breakup of the Columbia supercontinent in the NQOB need further study.

6. Conclusions

(1) The JBIF and associated metasedimentary rocks were deposited at 1.23–1.33 Ga.
(2) The metasediments are the products of intense chemical weathering and erosion. They were mainly derived from mafic

and intermediate igneous rocks of the Zhulongguan Group, coeval with the major detrital zircons recorded at the 1747 Ma tectono-thermal event. The subordinate Early-Mesoproterozoic detrital zircons and minor zircons with Archean ages were probably derived from the North Qilian area and the Archean basement in the neighboring old craton, respectively.

(3) The mid-Mesoproterozoic diabases were likely generated by partial melting of the transitional mantle.
(4) The JBIF was deposited in a continental margin sea within extensional setting.

References

Arnold, G.L., Anbar, A.D., Barling, J., Lyons, T.W., 2004. Molybdenum isotope evidence for widespread anoxia in Mid-Proterozoic oceans. Science 304, 87–90.
Asiedu, D.K., Suzuki, S., Nogami, K., Shibata, T., 2000. Geochemistry of lower cretaceous sediments, inner zone of Southwest Japan: constraints on provenance and tectonic environment. Geochem. J. 34, 155–173.
Basta, F.F., Maurice, A.E., Fontboté, L., Favarger, P.Y., 2011. Petrology and geochemistry of the banded iron formation (BIF) of WadiKarim and Um Anab, Eastern Desert, Egypt: implications for the origin of Neoproterozoic BIF. Precambrian Res. 187 (3), 277–292.
Bathia, M.R., 1983. Plate tectonics and geochemical composition of sandstones. J. Geol. 91, 611–627.
Bekker, A., Holland, H.D., Wang, P.L., Rumble, D.I.I.I., Stein, H.J., Hannah, J.L., Beukes, N.J., 2004. Dating the rise of atmospheric oxygen. Nature 427 (6970), 117–120.
Bekker, A., Slack, J.F., Planavsky, A., Krapež, B., Hofmann, A., Konhauser, K.O., Rouxel, O.J., 2010. Iron formation: the sedimentary product of a complex interplay among mantle, tectonic, oceanic, and biospheric processes. Econ. Geol. 105, 467–508.
Bhatia, M., Crook, K.W., 1986. Trace element characteristics of graywackes and tectonic setting discrimination of sedimentary basins. Contrib. Mineral. Petrol. 92, 181–193.
Black, L.P., Kamo, S.L., Williams, I.S., Mundil, R., Davis, D.W., Korsch, R.J., Foudoulis, C., 2003. The application of SHRIMP to Phanerozoic geochronology: a critical appraisal of four zircon standards. Chem. Geol. 200, 171–188.
Bock, B., McLennan, S.M., Hanson, G.N., 1998. Geoehemistry and provenance of the Middle Odovieian Astin Glen member (Normanskill Formation) and the Taconian Orogeny in New England. Sedimentology 45, 635–655.
Button, A., Brock, T.D., Cook, P.J., Eugster, H.P., Goodwin, A.M., James, H.L., Margulis, L., Nealson, K.H., Nriagu, J.O., Trendall, A.F., Walter, M.R., 1982. Sedimentary iron deposits evaporites and phosphorites: state of art report. In: Holland, H.D., Schidlowski, M. (Eds.), Mineral Deposits and the Evolution of the Biosphere. Springer-Verlag, pp. 259–273.
Canfield, D.E., 1998. A new model for Proterozoic ocean chemistry. Nature 396, 450–453.
Cawood, P.A., Nemchin, A.A., 2000. Provenance record of a rift basin: U/Pb ages of detrital zircons from the Perth Basin, Western Australia. Sediment. Geol. 134 (3), 209–234.
Che, Z.C., Sun, Y., 1996. The age of the Altun granulite facies complex and the basement of the Tarim Basin. Reg. Geol. China 1, 51–57 (in Chinese with English abstract).
Condie, K.C., 1997. Sources of Proterozoic mafic dykes swarms: constraints from Th/Ta and La/Yb ratios. Precambrian Res. 81, 3–14.
Cox, G.M., Halverson, G.P., Minarik, W.G., Le Heron, D.P., Macdonald, F.A., Bellefroid, E.J., Strauss, J.V., 2013. Neoproterozoic iron formation: an evaluation of its temporal, environmental and tectonic significance. Chem. Geol. 362, 232–249.
Cullers, R.L., 1995. The controls on the major- and trace-element evolution of shales, siltstones and sandstones of Ordovician to Tertiary age in the Wet Mountains region, Colorado, U.S.A. Chem. Geol. 123, 107–131.
Cullers, R.L., Bock, B., Guidotti, C., 1997. Elemental distributions and neodymium isotopic compositions of Silurian metasediments, western Maine, USA: redistribution of the rare earth elements. Geochim. Cosmochim. Acta 61, 1847–1861.
Ernst, R.E., Wingate, M.T.D., Buchan, K.L., Li, Z.X., 2008. Global record of 1600–700 Ma large igneous provinces (LIPs): implications for the reconstruction of the proposed Nuna (Columbia) and Rodinia supercontinents. Precambrian Res. 160, 159–178.

Faure, G., 1977. Principles of Isotope Geology. Smith and Wyllie Intermediate Geology SeriesJohn Wiley and Sons, Inc., New York, NY, United States, p. 47.

Fedo, C.M., Nesbitt, H.W., Young, G.M., 1995. Unraveling the effects of potassium metasomatism in sedimentary rocks and paleosols, with implications for paleoweathering conditions and provenance. Geology 23, 921–924.

Floyd, P.A., Leveridge, B.E., 1987. Tectonic environment of the Devonian Gramscatho basin, south Cornwall: framework mode and geochemical evidence from turbiditic sandstones. J. Geol. Soc. 144, 531–542.

Gross, G.A., 1965. Geology of iron deposits in Canada: general geology and evaluation of iron deposits. Geol. Surv. Can. Econ. Rep. 22, 1–181.

Gross, G.A., McLeod, C.R., 1980. A preliminary assessment of the chemical composition of iron formations in Canada. Can. Mineral. 18 (2), 223–229.

Gu, X.X., Liu, J.M., Zheng, M.H., Tang, J.X., Qi, L., 2002. Provenance and tectonic setting of the Proterozoic turbidites in Hunan, South China: geochemical evidence. J. Sediment. Res. 72, 393–407.

Guo, L.Y., Gan, Z.M., Li, H.M., 2002. Single-zircon U–Pb dating of the Liugouxia Granitic gneiss in the western segment of the North Qilian Mountains. Geol. China 29 (2), 126–128 (in Chinese with English abstract).

Hawkesworth, C.J., Turner, S.P., McDermott, F., Peate, D.W., van Calsteren, P., 1997. U–Th isotopes in arc magmas: implications for element transfer from subducted crust. Science 276, 551–555.

Hayashi, K.-I., Fujisawa, H., Holland, H.D., Ohmoto, H., 1997. Geochemistry of 1.9 Ga sedimentary rocks from northeastern Labrador, Canada. Geochim. Cosmochim. Acta 61, 4115–4137.

He, S.P., Li, R.S., Wang, C., Yu, P.S., Gu, P.Y., Shi, C., 2010. Geochronology of gneissic plagioclase-amphibolite from Beidahe Group complex in western segment of Qilian Mountains, China. Geol. Bull. China 29 (9), 1275–1280 (in Chinese with English abstract).

Herron, M.M., 1988. Geochemical classifications of terrigenous sands and shales from core or log data. J. Sediment. Petrol. 58, 820–829.

Holland, H., 1984. The Chemical Evolution of the Atmosphere and Oceans. Princeton University Press, New York (582 pp.).

Holland, H., 2003. The geologic history of seawater. Treatise Geochem. 6, 583–625.

Holland, H., 2005. Sedimentary mineral deposits and the evolution of Earth's near-surface environments. Econ. Geol. 100, 1489–1509.

Hoskin, P.W., 2005. Trace-element composition of hydrothermal zircon and the alteration of Hadean zircon from the Jack Hills, Australia. Geochim. Cosmochim. Acta 69 (3), 637–648.

Hoskin, P.W., Schaltegger, U., 2003. The composition of zircon and igneous and metamorphic petrogenesis. Rev. Mineral. Geochem. 53 (1), 27–62.

Hou, K.J., Li, Y.J., Tian, Y.R., 2009. In situ U–Pb zircon dating using laser ablation-multi ion counting-ICP-MS. Mineral Deposits 28 (4), 481–492 (in Chinese with English abstract).

Hu, J., Gong, W., Wu, S., Liu, Y., Liu, S., 2014. LA-ICP-MS zircon U–Pb dating of the Langshan Group in the northeast margin of the Alxa block, with tectonic implications. Precambrian Res. 255, 756–770.

Huang, H., Niu, Y., Nowell, G., Zhao, Z., Yu, X., Mo, X., 2015. The nature and history of the Qilian Block in the context of the development of the Greater Tibetan Plateau. Gondwana Res. 28, 209–224.

Huston, D.L., Logan, G.A., 2004. Barite, BIFs and bugs: evidence for the evolution of the Earth's early hydrosphere. Earth Planet. Sci. Lett. 220, 41–55.

Ilyin, A.V., 2009. Neoproterozoic banded iron formations. Lithol. Miner. Resour. 44, 78–86.

Irvine, T., Baragar, W., 1971. A guide to the chemical classification of the common volcanic rocks. Can. J. Earth Sci. 8 (5), 523–548.

Isley, A.E., Abbott, D.H., 1999. Plume-related mafic volcanism and the deposition of banded iron formation. Journal of Geophysical Research. Solid Earth 104 (B7), 15461–15477.

James, H.L., 1992. Precambrian iron-formations: nature, origin, and mineralogic evolution from sedimentation to metamorphism. In: Wolf, K.H., Chilingarian, G.V. (Eds.), Diagensis III. Developments in Sedimentology 47, pp. 543–589.

Ker, C.M., Yang, H.J., Zhang, J.X., Shau, Y.H., Chieh, C.J., Meng, F.C., Takazawa, E., You, C.F., 2015. Compositional and Sr–Nd–Hf isotopic variations of Baijingsi eclogites from the North Qilian orogen, China: causes, protolith origins, and tectonic implications. Gondwana Res. 28, 721–734.

Klein, C., 2005. Some Precambrian banded iron-formations (BIFs) from around the world: their age, geologic setting, mineralogy, metamorphism, geochemistry, and origin. Am. Mineral. 90, 1473–1499.

Kump, L.R., Seyfried, W.E., 2005. Hydrothermal Fe fluxes during the Precambrian: effect of low oceanic sulfate concentrations and low hydrostatic pressure on the composition of black smokers. Earth Planet. Sci. Lett. 235, 654–662.

Lascelles, D.F., 2014. Plate tectonics caused the demise of banded iron formations. Appl. Earth Sci. (Trans. Inst. Min. Metall. B) 122 (4), 230–241.

LeRoex, A.P., Dick, H.J.B., Erlank, A.J., Reid, A.M., Reay, F.A., Hart, S.R., 1983. Geochemistry, mineralogy and petrogenesis of lavas erupted along the southwest Indian Ridge between the Bouvet triple junction and 11 degrees east. J. Petrol. 24, 267–318.

Li, H.K., Lu, S.N., Xiang, Z.Q., Zhou, H.Y., Li, H.M., Liu, D.Y., Song, B., Zheng, J.K., Gu, Y., 2007. SHRIMP U–Pb geochronological research on detrital zircons from the Beidahe complex-group in the western segment of the North Qilian Mountains, Northwest China. Geol. Rev. 53 (1), 132–140 (in Chinese with English abstract).

Li, H.K., Lu, S., Su, W.B., Xiang, Z.Q., Zhou, H.Y., Zhang, Y., 2013. Recent advances in the study of the Mesoproterozoic geochronology in the North China Craton. J. Asian Earth Sci. 72, 216–227.

Li, H.M., Zhang, Z.J., Li, L.L., Zhang, Z.C., Chen, J., Yao, T., 2014. Types and general characteristics of the BIF-related iron deposits in China. Ore Geol. Rev. 57, 264–287.

Li, H.M., Li, L.X., Yang, X.Q., Cheng, Y.B., 2015a. Types and geological characteristics of iron deposits in China. J. Asian Earth Sci. 103, 2–22.

Li, L.X., Li, H.M., Xu, Y.X., Chen, J., Yao, T., Zhang, L.F., Yang, X.Q., Liu, M.J., 2015b. Zircon growth and ages of migmatites in the Algoma-type BIF-hosted iron deposits in Qianxi Group from eastern Hebei Province, China: timing of BIF deposition and anatexis. J. Asian Earth Sci. http://dx.doi.org/10.1016/j.jseaes.2015.02.007.

Liu, H.S., Li, Q.L., Yu, P.S., Wu, J.R., 1998. Geological characteristic and genesis of the Jingtieshan-type iron–copper deposits. Mineral Deposits 17 (1), 25–35 (in Chinese with English abstract).

Lu, S.N., Li, H.K., Zhang, C.L., Niu, G.H., 2008. Geological and geochronological evidence for the Precambrian evolution of the Tarim Craton and surrounding continental fragments. Precambrian Res. 160 (1–2), 94–107.

Lyons, T.W., Reinhard, C.T., Planavsky, N.J., 2014. The rise of oxygen in Earth's early ocean and atmosphere. Nature 506 (20), 307–315.

Mao, J.W., Zhao, Z.C., Yang, J.M., Song, B., Wu, M.B., Zuo, G.C., 1997. Single grain zircon dating of the Precambrian strata in west section of the North Qilian Mountain and its geological significance. Chin. Sci. Bull. 42 (13), 1414–1417 (in Chinese with English abstract).

Mao, J.W., Zhang, Z.C., Yang, J.M., Zuo, G.C., Zhang, Z.H., Ye, D.J., Wang, Z.L., Ren, F.S., Zhang, Y.J., Peng, C., Liu, Y.Z., Jiang, M., 2003. The Metallogenic Series and Prospecting Assessment of Copper, Gold, Iron and Tungsten Polymetallic Ore Deposits in the West Sector of the Northern Qilian Mountains. Geological Publishing House, Beijing, pp. 157–242 (in Chinese).

Mao, J.W., Zhang, Z.H., Pei, R.F., 2012. Mineral Deposit Models in China. Geological Publishing House, Beijing, pp. 218–223 (in Chinese).

McDonough, W.F., Sun, S.S., 1985. Isotopic and geochemical systematics in Tertiary–recent basalts from Southeastern Australia and implication for the subcontinental lithosphere. Geochim. Cosmochim. Acta 49, 2051–2067.

McLennan, S.M., 2001. Relationships between the trace element composition of sedimentary rocks and upper continental crust. Geochem. Geophys. Geosyst. 2 (4), 1021–1024.

McLennan, S.M., Taylor, S.R., McCulloch, M.T., Maynard, J.B., 1990. Geochemical and Nd–Sr isotopic composition of deep-sea turbidites: crustal evolution and plate tectonic associations. Geochim. Cosmochim. Acta 54, 2015–2050.

McLennan, S.M., Hemming, S., Mcdaniel, D.K., Hanson, G.N., 1993. Geochemical approaches to sedimentation, provenance, and tectonics. In: Johnson, M.J., Basu, A. (Eds.), Processes Controlling the Composition of Clastic Sediments. Geological Society of America, Boulder, Colorado, pp. 21–40 (Spec. Paper 284).

Mclennan, S.M., Hemming, S., Taylor, S.R., Eriksson, K.A., 1995. Early Proterozoic crustal evolution: geochemical and Nd–Pb isotopic evidence from metasedimentary rocks, southwestern North America. Geochim. Cosmochim. Acta 59, 1153–1177.

Meert, J.G., 2014. Strange attractors, spiritual interlopers and lonely wanderers: the search for pre-Pangean supercontinents. Geosci. Front. 5, 155–166.

Meschede, M., 1986. A method of discrimination between different types of mid ocean ridge basalts and continental tholeiites with the Nb–Zr–Hf diagram. Chem. Geol. 56, 207–218.

Nagarajan, R., Roy, P.D., Jonathan, M.P., Lozano, R., Kessler, F.L., Prasanna, M.V., 2014. Geochemistry of Neogene sedimentary rocks from Borneo Basin, East Malaysia: paleoweathering, provenance and tectonic setting. Chem. Erde-Geochem. 74 (1), 139–146.

Nance, R.D., Murphy, J.B., Santosh, M., 2014. The supercontinent cycle: a retrospective essay. Gondwana Res. 25, 4–29.

Nesbitt, H.W., Young, G.M., 1982. Early Proterozoic climates and plate motions inferred from major element chemistry of lutites. Nature 299, 715–717.

Pearce, J.A., Cann, J.R., 1973. Tectonic setting of basalts rocks determined using trace element analyses. Earth Planet. Sci. Lett. 19, 290–300.

Pearce, J.A., Norry, M.J., 1979. Petrogenetic implications of Ti, Zr, Y and Nb variations in volcanic rocks. Contrib. Mineral. Petrol. 69, 33–47.

Planavsky, N.J., Mcgoldrick, P., Scott, C.T., Li, C., Reinhard, C.T., Kelly, A.E., Chu, X.l., Bekker, A., Love, G.D., Lyons, T.W., 2011. Widespread iron-rich conditions in the Mid-Proterozoic ocean. Nature 477 (7365), 448–451.

Poulton, S.W., Canfield, D.E., 2011. Ferruginous conditions: a dominant feature of the ocean through Earth's history. Elements 7, 107–112.

Poulton, S.W., Fralick, P.W., Canfield, D.E., 2004. The transition to a sulphidic ocean 1.84 billion years ago. Nature 43, 173–177.

Pufahl, P.K., Pirajno, F., Hiatt, E., 2013. Riverine mixing and fluvial iron formation: a new type of Precambrian biochemical sediment. Geology 41 (12), 1235–1238.

Reinhard, C.T., Planavsky, N.J., Robbins, L.J., Partin, C.A., Gill, B.C., Lalonde, S.V., Bekker, A., Konhauser, K.O., Lyons, T.W., 2013. Proterozoic ocean redox and biogeochemical stasis. PNAS 110, 5357–5362.

Richards, S.M., 1966. The banded iron formations at Broken Hill, Australia, and their relationship to the lead–zinc orebodies. Econ. Geol. 61 (1), 72–96.

Ringwood, A.E., 1975. Composition and Petrology of the Earth's Mantle. McGrawHill, New York, pp. 1–618.

Rogers, J.J.W., Santosh, M., 2002. Configuration of Columbia, a Mesoproterozoic supercontinent. Gondwana Res. 5, 5–22.

Rogers, J.J.W., Santosh, M., 2009. Tectonics and surface effects of the supercontinent Columbia. Gondwana Res. 15, 373–380.

Roser, B.P., Korsch, R.J., 1988. Provenance signatures of sandstone mudstone suites determined using discriminant function analysis of major-element data. Chem. Geol. 67, 119–139.

Rudnick, R.L., Gao, S., 2003. The composition of the continental crust. In: Rudnick, R.L. (Ed.), The Crust. Elsevier-Pergamon, Oxford, pp. 1–64.

Sifeta, K., Roser, B.P., Kimura, J.I., 2005. Geochemistry, provenance, and tectonic setting of Neoproterozoic metavolcanic and metasedimentary units, Werri area, Northern Ethiopia. J. Afr. Earth Sci. 41 (3), 212–234.

Slack, J.F., Grenne, T., Bekker, A., 2009. Seafloor-hydrothermal Si–Fe–Mn exhalites in the Pecos greenstone belt, New Mexico, and the redox state of ca. 1720 Ma deep seawater. Geosphere 5, 302–314.

Smith, R.E., 1976. Comments on the use of Ti, Zr, Y, Sr, K, P and Na in classification of basaltic magmas. Earth Planet. Sci. Lett. 32, 114–120.

Song, S., Niu, Y., Su, L., Xia, X., 2013. Tectonics of the North Qilian orogen, NW China. Gondwana Res. 23 (4), 1378–1401.

Sun, S.S., McDonough, W.F., 1989. Chemical and isotopic systematics of oceanic basalts: implications for mantle composition and processes. Geol. Soc. Lond., Spec. Publ. 42 (1), 313–345.

Sun, H.T., Wu, J.R., Yu, P.S., Li, J.P., 1998. Geology, geochemistry and sulfur isotope composition of the Late Proterozoic Jingtieshan (superior-type) hematite–jasper–barite iron ore deposits associated with strata-bound Cu mineralization in the Gansu Province, China. Mineral. Deposita 34, 102–112.

Taylor, S.R., McLennan, S.M., 1985. The Continental Crust: Its Composition and Evolution. Blackwell Scientific Publishers, Oxford.

Wan, Y.S., Dong, C.Y., Xie, H.Q., Wang, S.J., Song, M.C., Xu, Z.Y., Wang, S.Y., Zhou, H.Y., Ma, M.Z., Liu, D.Y., 2012. Formation ages of early Precambrian BIFs in the North China Craton: SHRIMP zircon U–Pb dating. Acta Geol. Sin. 86, 1447–1478 (in Chinese with English abstract).

Wang, Q., Yang, D., Xu, W., 2012. Neoproterozoic basic magmatism in the southeast margin of North China Craton: evidence from whole-rock geochemistry, U–Pb and Hf isotopic study of zircons from diabase swarms in the Xuzhou–Huaibei area of China. Sci. China Earth Sci. 55 (9), 1461–1479.

Wang, Z.M., Han, C.M., Su, B.X., Sakyi, P.A., Malaviarachchi, S.P., Ao, S.J., Wang, L.J., 2013. The metasedimentary rocks from the eastern margin of the Tarim Craton: petrology, geochemistry, zircon U–Pb dating, Hf isotopes and tectonic implications. Lithos 179, 120–136.

Wang, W., Liu, S., Santosh, M., Zhang, L., Bai, X., Zhao, Y., Zhang, S., Guo, R., 2015. 1.23 Ga mafic dykes in the North China Craton and their implications for the reconstruction of the Columbia supercontinent. Gondwana Res. 27, 1407–1418.

Willis, K.M., Stern, R.J., Claur, N., 1988. Age and geochemistry of Late Precambrian sediments of the Hammamat series from the northeastern desert of Egypt. Precambrian Res. 42, 173–187.

Winchester, J.A., Floyd, P.A., 1977. Geochemical discrimination of different magma series and their differentiation products using immobile elements. Chem. Geol. 20, 325–343.

Wingate, M.T.D., Campbell, I.H., Compston, W., Gibson, G.M., 1998. Ion microprobe U–Pb ages for Neoproterozoic basaltic magmatism in south-central Australia and implications for the breakup of Rodinia. Precambrian Res. 87, 135–159.

Wu, C., Gao, Y., Frost, B.R., Robinson, P.T., Wooden, J.L., Wu, S., Chen, Q., Lei, M., 2011. An early Palaeozoic double-subduction model for the North Qilian oceanic plate: evidence from zircon SHRIMP dating of granites. Int. Geol. Rev. 53 (2), 157–181.

Xia, Z.C., Xia, L.Q., Xu, X.Y., 1996. The Late-Proterozoic–Cambrian active continental rift volcanism in Northern Qilian Mountains. Acta Geosci. Sin. 17 (3), 282–291 (in Chinese with English abstract).

Xia, L.Q., Xia, Z.C., Zhao, J.T., Xu, X.Y., Yang, H.Q., Zhao, D.H., 1999. Determination of properties of Proterozoic continental flood basalts of western part from North Qilian Mountains. Sci. China (Ser. D) 42 (5), 506–514.

Xia, L.Q., Xia, Z.C., Xu, X.Y., 2003. Magmagenesis in the Ordovician backarc basins of the NQOB Mountain, China. Geol. Soc. Am. Bull. 115, 1510–1522.

Xu, Z.Q., Xu, H.F., Zhang, J.X., 1994. The Zoulangnanshan Caledonian subductive complex in the Northern Qilian Mountains and its dynamics. Acta Geol. Sin. 68, 1–15 (in Chinese with English abstract).

Xu, X.C., Yue, S.C., Liu, Y., Zhou, T.F., 1996. The time and petrochemical characteristic of volcanics of Zhulongguan Group in Zoulangnanshan, Gansu. Geol. Anhui 6 (4), 1–6 (in Chinese with English abstract).

Xu, D.R., Wang, Z.L., Chen, H.Y., Hollings, P., Jansen, N.H., Zhang, Z.C., Wu, C.J., 2014. Petrography and geochemistry of the Shilu Fe–Co–Cu ore district, South China: implications for the origin of a Neoproterozoic BIF system. Ore Geol. Rev. 57, 322–350.

Xue, C.J., Ji, J.S., Zhang, L.C., Lu, D.R., Liu, H.S., Li, Q.L., 1997. The Jingtieshan submarine exhalative-sedimentary iron–copper deposit in north Qilian Mountain. Mineral Deposits 16 (1), 21–30 (in Chinese with English abstract).

Yang, H.Q., Zhao, H.D., 1999. Age of Cu-bearing banded iron formation in Jingtieshan, Gansu. Northwest Geosci. 20 (1), 1–3 (in Chinese with English abstract).

Yang, H.Z., Lu, J.W., Yao, Y., Jia, Z.L., Deng, R.D., Wang, D.K., 1991. The geological characteristic of Jingtieshan iron deposit and its genesis. Mineral Deposit Monogr. 1–231 (in Chinese).

Yang, X.Q., Zhang, Z.H., Duan, S.G., Zhao, X.M., 2015. Petrological and geochemical features of the Jingtieshan banded iron formation (BIF): a unique type of BIF from the Northern Qilian Orogenic Belt, NW China. J. Asian Earth Sci. http://dx.doi.org/10.1016/j.jseaes.2015.03.024.

Zhai, M.G., 2014. Multi-stage crustal growth and cratonization of the North China Craton. Geosci. Front. 5, 457–469.

Zhai, M.G., Santosh, M., 2013. Metallogeny of the North China Craton: link with secular changes in the evolving Earth. Gondwana Res. 24, 275–297.

Zhang, Z.C., Mao, J.W., Yang, J.M., Zuo, G.C., Wu, M.B., 1998. Discovery of Middle Proterozoic ophiolite in the west part of North Qilian Mountains and its geological significance. Bull. Mineral. Petrol. Geochem. 17 (2), 114–118.

Zhang, Z.C., Zhou, M.F., Robinson, P.T., Mao, J.W., Yang, J.M., Zuo, G.C., 2001. SHRIMP dating of the Aoyougou ophiolite in the west sector of the north Qilian Mountains and its geological significance. Acta Petrol. Sin. 17 (2), 222–226 (in Chinese with English abstract).

Zhang, L.Y., Qu, X.M., Xin, H.B., 2008. Geochemical characteristics, zircon U–Pb LA-ICP-MS ages of medium-acid dykes in the Huashugou iron–copper deposit, Jingtieshan orefield and their geological significances. Geol. Rev. 54 (2), 253–262 (in Chinese with English abstract).

Zhang, S.H., Zhao, Y., Yang, Z.Y., He, Z.F., Wu, H., 2009. The 1.35 Ga diabase sills from the northern North China Craton: implications for breakup of the Columbia (Nuna) supercontinent. Earth Planet. Sci. Lett. 288 (3), 588–600.

Zhang, X.J., Zhang, L.C., Xiang, P., Wan, B., Pirajno, F., 2011. Zircon U–Pb age, Hf isotopes and geochemistry of Shuichang algoma-type banded iron-formation, North China Craton: constraints on the ore-forming age and tectonic setting. Gondwana Res. 20, 137–148.

Zhang, L.C., Zhai, M.G., Zhang, X.J., Xiang, P., Dai, Y.P., Wang, C.L., Pirajno, F., 2012. Formation age and tectonic setting of the Shirengou Neoarchean banded iron deposit in eastern Hebei Province: constraints from geochemistry and SIMS zircon U–Pb dating. Precambrian Res. 222, 325–338.

Zhang, Z.C., Hou, T., Santosh, M., Li, H.M., Li, J.W., Zhang, Z.H., Song, X.Y., Wang, M., 2014. Spatio-temporal distribution and tectonic settings of the major iron deposits in China: an overview. Ore Geol. Rev. 57, 247–263.

Zhao, G.C., Cawood, P.A., Wilde, S.A., Sun, M., 2002. A review of the global 2.1–1.8 Ga orogens: implications for a pre-Rodinia supercontinent. Earth Sci. Rev. 59, 125–162.

Zhao, D.H., Zhang, H.Q., Liu, Y.L., Wang, F.C., 2003a. Discussion on metallogenic age of Huashugou copper deposit in Gansu. Mineral Deposits 22 (2), 134–140 (in Chinese with English abstract).

Zhao, G.C., Sun, M., Wilde, S.A., Li, S.Z., 2003b. Assembly, accretion and breakup of the paleo-Mesoproterozoic Columbia supercontinent: records in the North China Craton. Gondwana Res. 6, 417–434.

Zhao, G.C., Sun, M., Wilde, S.A., Li, S., 2004. A paleo-Mesoproterozoic supercontinent: assembly, growth and breakup. Earth Sci. Rev. 67, 91–123.

Zhou, T.F., Yue, S.C., 1999. Geochemistry and metallogenesis of the Huashugou copper (iron) deposit in the Northern Qilian Mountain. Geol. Prospect. 35 (3), 23–29 (in Chinese with English abstract).

Zuo, G.C., Liu, Y.K., Zhang, C., 2002. Tectono-stratigraphic characteristics of continent crustal remnants in central-western sector of the North Qilian orogen. Chin. J. Geol. 37 (3), 302–312 (in Chinese with English abstract).